

Two-temperature scales in the triangular-lattice Heisenberg antiferromagnet

Lei Chen,¹ Dai-Wei Qu,¹ Han Li,¹ Bin-Bin Chen,^{1,2} Shou-Shu Gong,¹ Jan von Delft,² Andreas Weichselbaum,^{3,2,*} and Wei Li^{1,4,†}

¹Department of Physics, Key Laboratory of Micro-Nano Measurement-Manipulation and Physics (Ministry of Education), Beihang University, Beijing 100191, China

²Munich Center for Quantum Science and Technology (MCQST), Arnold Sommerfeld Center for Theoretical Physics (ASC) and Center for NanoScience (CeNS), Ludwig-Maximilians-Universität München, Fakultät für Physik, D-80333 München, Germany.

³Department of Condensed Matter Physics and Materials Science, Brookhaven National Laboratory, Upton, New York 11973-5000, USA

⁴International Research Institute of Multidisciplinary Science, Beihang University, Beijing 100191, China

(Dated: April 12, 2019)

The anomalous thermodynamic properties of the paradigmatic frustrated spin-1/2 triangular lattice Heisenberg antiferromagnet (TLH) has remained an open topic of research over decades, both experimentally and theoretically. Here we further the theoretical understanding based on the recently developed, powerful exponential tensor renormalization group (XTRG) method on cylinders and stripes in a quasi one-dimensional (1D) setup, as well as a tensor product operator approach directly in 2D. The observed thermal properties of the TLH are in excellent agreement with two recent experimental measurements on the virtually ideal TLH material $\text{Ba}_8\text{CoNb}_6\text{O}_{24}$. Remarkably, our numerical simulations reveal two crossover temperature scales, at $T_l/J \sim 0.20$ and $T_h/J \sim 0.55$, with J the Heisenberg exchange coupling, which are also confirmed by a more careful inspection of the experimental data. We propose that in the intermediate regime between the low-temperature scale T_l and the higher one T_h , the “rotonlike” excitations are activated with a strong chiral component and a large contribution to thermal entropies. Bearing remarkable resemblance to the renowned roton thermodynamics in liquid helium, these gapped excitations suppress the incipient 120° order that emerges for temperatures below T_l .

Introduction. The triangular lattice Heisenberg (TLH) model is arguably the most simple prototype of a frustrated quantum spin system. It has attracted wide attention since Anderson’s famous proposal of a resonating valence bond (RVB) spin liquid state [1]. The competition between RVB liquid versus semiclassical Néel solid states raised great interest. After decades of research, it is now widely accepted that the TLH has noncollinear 120° order at $T = 0$, with a spontaneous magnetization [2], $m \simeq 0.205$ [3, 4]. Nevertheless, the TLH has long been noticed to possess *anomalous* thermodynamic properties [5], in the sense that thermal states down to rather low-temperature regimes behave more as a system with no indication of an ordered ground state [6, 7].

Bipartite-lattice Heisenberg antiferromagnets (AFs) such as the square-lattice Heisenberg (SLH) model, develop a semiclassical magnetic order at $T = 0$ which is “melted” at any finite temperature according to the Mermin-Wagner theorem [8]. Nevertheless, the groundstate Néel order strongly influences low-temperature thermodynamics in the so-called renormalized classical (RC) regime [9, 10], where the spin-spin correlation length ξ increases exponentially as T decreases [11–14].

In contrast, the thermodynamics of the TLH strikingly differs in many respects from that of SLH. Based on high-temperature series expansion (HTSE) results, both models show c_V peaks at similar temperatures, $T_h \simeq 0.55$ (TLH) and $T_s \simeq 0.6$ (SLH). The SLH enters the RC regime for $T \lesssim T_s$ [11, 12], whereas the TLH shows no signature for incipient order and possesses anomalously large entropies at temperatures below T_h [6].

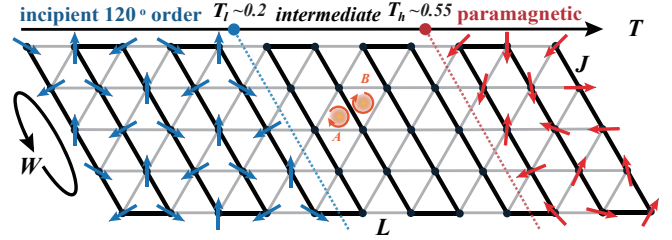


FIG. 1. (Color online) Uniform TLH with nearest-neighbor (NN) coupling $J=1$ (which thus sets the unit of energy) and lattice spacing $a=1$, with three schematically depicted distinct regimes, separated by two cross-over temperature scales, T_l and T_h : an incipient 120° ordered regime for $T < T_l$ (left), a paramagnetic regime for $T > T_h$ (right), an intermediate regime (center), which is explored in detail in this paper. The thick black line indicates the 1D snake order adopted in the MPO-based XTRG. When the system is wrapped into a cylinder along the tilted left arrow, this is referred to as YC geometry. The clockwise oriented circles in the center of the system indicate chiral operators, $\chi \equiv 2^3 \cdot S_a \cdot (S_b \times S_c)$, acting on the enclosing triangle of sites (a, b, c) in the order of the arrows, as used for the calculation of chiral correlations between the triangle pair A-B.

The classical SLH and TLH models have a similar spin stiffness ρ_s , and thus a similar constant, $C_\xi \sim \rho_s$, in the correlation length, $\xi \sim \exp(\frac{C_\xi}{T})$, as well as in the static structure factor at the ordering wave vector, $S(K) \sim \exp(\frac{2C_\xi}{T})$, with $C_\xi = 2\pi\rho_s = 1.571$ (SLH) [15] and $C_\xi = 4\pi\rho_s = 1.748$ (TLH) [5, 16, 17] in units of spin coupling J . However, the constant C_ξ is significantly renormalized by quantum fluctuations. For the SLH, the constant is reduced by about 30% to $C_\xi \sim 1.13$,

while in the TLH it is reduced by an order of magnitude down to $C_\xi \sim 0.1$ [5, 6]. The energy scale $E_{RC} \equiv 2C_\xi$ naturally represents the onset of RC behavior and thus incipient order. Recent sign-blessing bold diagrammatic Monte Carlo (BDMC) simulations still show that the thermal states down to the lowest accessible temperatures $T = 0.375$ “extrapolate” to a disordered ground state via a quantum-to-classical correspondence [7].

Here, we exploit two renormalization group (RG) techniques based on thermal tensor network states (TNSs) [18–20]: the exponential tensor RG (XTRG) which we recently introduced based on one-dimensional (1D) matrix product operators (MPOs) [20], and a tensor product operator (TPO) approach [18]. XTRG is employed to simulate the TLH down to temperatures $T < 0.1$ on $YC W(\times L)$ geometries (see Fig. 1) up to width $W = 6$ with default $L = 2W$, and open strips [OS $W(\times L)$] with fully open boundary conditions (OBCs) and default $L = W$ [21].

TLH thermodynamics. In Fig. 2 we present our thermodynamical results from XTRG on cylinder (YC) and open geometries (OS), as defined earlier. In Fig. 2(a), we observe from YC5, OS6, and YC6 data that, besides a high temperature round peak at $T_h \sim 0.55$, our YC data exhibit another peak (shoulder for OS6) at $T_l \sim 0.2$. On YCs, the peak position T_l stays nearly the same when increasing W from 5 to 6, also consistent with the shoulder in OS6 as well as in the experimental data. At the same time, the low-temperature peak becomes slightly weakened, yet towards the experimental data. When compared to the two virtually coinciding experimental data sets, YC6, TPO, earlier HTSE [5], and latest Padé [6,6] data [36] all agree well for $T \gtrsim T_h$ and reproduce the round peak of c_V at T_h .

The remarkable agreement of finite-size XTRG with experimental measurements can be ascribed to a short correlation length $\xi \lesssim 1$ lattice spacing for $T \gtrsim 0.4$ [21]. Deviations from experiment only take place below T_l , suggesting significant finite-size effects due to larger ξ in that regime. Moreover, we have checked the dependence of T_l on the cylinder length L for YC6, and find that the lower peak even gets slightly enhanced as L increases. In addition to YC and OS geometries, simulations on X cylinders also lead to the same scenario [21].

In Fig. 2(b), we present our data on thermal entropy, again directly juxtaposed with experimental as well as previous theoretical results. Whereas the YC5 data deviate at $T \lesssim 0.3$ due to finite-size effects, we observe good agreement between the two experimental data sets with our TPO results down to T_l , and with $W = 6$ data (OS6 and YC6) down to the lowest temperatures in the measurements. Notably, the thermal entropy per site S is about 1/3 of the high- T limit, $S_\infty = \ln 2$, at temperatures as low as $T \simeq 0.2$ where, for comparison, for SLH S is almost zero at the same temperature [6]. We emphasize that Fig. 2(b) is a direct comparison without any fitting, since the only parameter J has also been determined and thus fixed as 1.66 K in the experiments [36, 37]. Nevertheless, since the experimental data of S are determined by integrating c_V/T ,

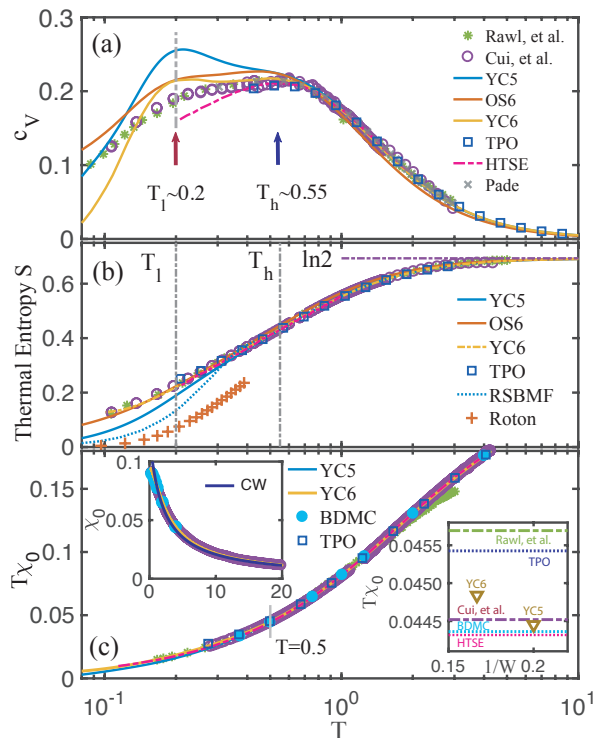


FIG. 2. (Color online) Simulated thermodynamics in comparison to experimental measurements, Cui *et al.* (2018) [37] and Rawl *et al.* (2017) [36], as well as earlier numerical results. The YC and OS data are obtained via XTRG by retaining up to $D^* = 1000$ multiplets [$D \sim 4000$ U(1) states], and by a TPO method [21] on infinite lattices, keeping up to 40 bond states. (a) Specific heat, c_V , results benchmarked against HTSE [5, 36] and experimental curves. (b) The thermal entropy S vs T , together with the reconstructed Schwinger boson mean field (RSBMF) [38], and “roton” contributions [16]. (c) Uniform magnetic susceptibility $T\chi_0$ vs T , shown with BDMC data [7]. The left top inset compares χ_0 to Curie-Weiss (CW) $\chi_0 = C/(T+\theta)$ in a wide temperature range, where $C = 1/4$ and $\theta = 2.06$. In the right bottom inset we further compare various $T\chi_0$ values at $T = 0.5$. The magnetic moment per Co is assumed $\simeq 2\mu_B$, with Landé factor $g \simeq 4.13$ [37].

starting from the lowest accessible temperature T_x , systematic vertical shifts for the curves from Refs. [36] and [37] are necessary to reach the known large- T limits. This results in residual entropies of $S(T_x) = 0.045$ and 0.06 at temperatures $T_x = 0.06$ and 0.08 K, for Refs. [36] and [37], respectively. Note that the large entropy due to quantum frustration at low T is not properly described in previous theories, e.g., RSBMF [38, 39] as shown in Fig. 2(b).

Figure 2(c) presents our results for the average magnetic susceptibility. Both data sets, YC5 and YC6, agree quantitatively with the experimental results, as well as HTSE data [5], from high temperatures down to $T \lesssim 0.1$, well beyond state-of-the-art BDMC results that reach down to $T = 0.375$ [7]. In the left top inset of Fig. 2(c), we also include a Curie-Weiss (CW) fit for $T \gtrsim 1$, resulting in the positive Weiss constant $\theta \approx 2J$. In the right bottom inset, we compare the $T\chi_0$ value

at $T = 0.5$, and find the various numerical and experimental results all agree, up to three significant digits.

Two-temperature scales. As schematically depicted in Fig. 1, we uncover a two-temperature-scale scenario in the TLH. This confirms that the 120° order plus magnon excitations is not sufficient to describe TLH thermodynamics. References [40, 41] argued that the TLH also has additional types of excitations which are gapped, with the minimum of their quadratic dispersion at finite momentum, and referred to these as “rotonlike excitations” (RLEs), since their dispersions are reminiscent of that known for vortexlike excitations in He^4 [42]. Excitations with this type of dispersion have recently also been observed in neutron scattering experiments of TLH materials [43, 44]. RLEs evidently play an important role in the intermediate-temperature regime in Fig. 1, but their precise nature has not yet been fully elucidated.

RLEs, although missed in the linear spin-wave theory, can be well captured by including $1/S$ corrections in calculating the magnon dispersions [41, 45, 46] and dynamical correlations [47, 48]. Other proposals have also been put forward to understand RLEs, including the vortex-antivortex excitation [49] with signatures already in the classical TLH phase diagram versus finite temperature [50–53], (nearly deconfined) spinon-antispinon pair [16, 40, 54], and magnon-interaction-stabilised excitations [47, 55, 56].

First, the RLE quadratic band with a finite gap $\Delta \sim 0.55 J$ contributes to a very prominent peak in the density of states around Δ [16]. This coincides with the high-temperature scale $T_h \sim \Delta$ here. Therefore a possible connection of RLEs to the thermodynamic anomaly in TLH has been suggested earlier [16, 46]. Second, the RLEs themselves only start to significantly contribute to the entropy above T_l [‘Roton’ entry in Fig. 2(b), with data taken from Ref. [16]]. This suggests that the RLEs are activated in the intermediate temperature regime, i.e., $T_l \lesssim T \lesssim T_h$. Consequently, the onset of incipient magnetic order is postponed to a clearly lower temperature $T_l \sim 0.2$, which is remarkably close to previous HTSE studies, where $E_{\text{RC}} \sim 0.2 J$ sets the energy scale of classical correlation [5] as discussed earlier.

Spin structure factors. In order to shed light into the spin configurations across the intermediate regime, we turn to the temperature dependent static structure factor, $S(q) \equiv \sum_j e^{-iq \cdot r_{0j}} \langle \mathbf{S}_0 \cdot \mathbf{S}_j \rangle_T$ where $r_{0j} \equiv r_j - r_0$ with r_j the lattice location of site j , and $S(q) \in \mathbb{R}$ due to lattice inversion symmetry. There are two further high-symmetry points of interest, $q = K$ and M , as marked in Fig. 3(a). Up to symmetric reflections, $K \equiv (\frac{2\pi}{3}, \frac{2\pi}{\sqrt{3}})$ relates to 120° non-collinear order, whereas $M \equiv (0, \frac{2\pi}{\sqrt{3}})$ relates to nearest-neighbor (stripe) AF correlations. The latter have also been related to RLEs which feature band minima at the M points [40, 41, 57].

In Figs. 3(a-d) we show the overall landscape of $S(q)$. With decreasing temperature, $S(q)$ changes from rather featureless in Fig. 3(a), to showing bright regions in the vicinity of the six equivalent K points as well as enhanced intensity at the M points at $T \sim T_h$ in Fig. 3(b). Even at $T \sim T_l$ in Fig. 3(c), one

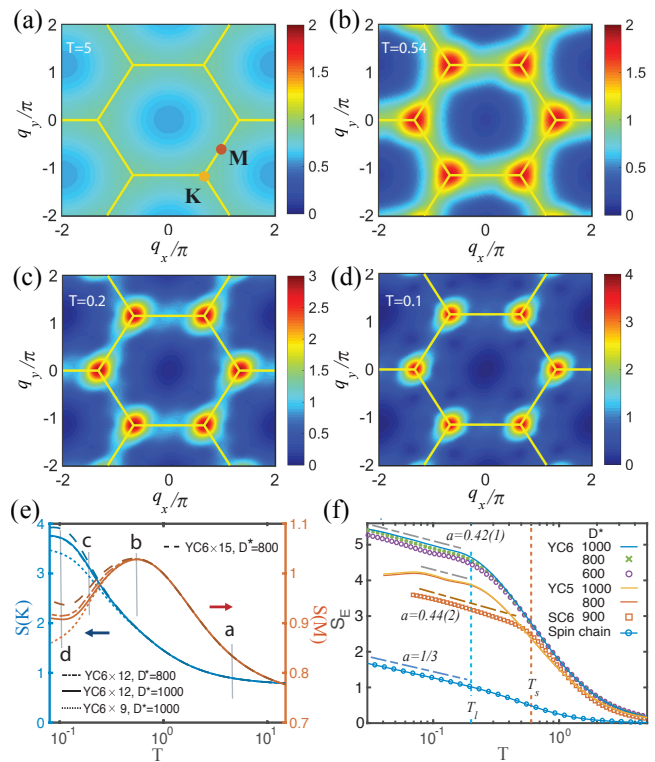


FIG. 3. (Color online) (a-d) Structure factor on $Y\text{C}6 \times 12$ lattice, i.e., with q_y pointing along the direction of the cylinder, at temperatures $T = 5, 0.54, 0.2$, and 0.1 , respectively, [vertical gray lines in (e)]. (e) $S(q)$ vs T at momenta $q = K$ and M where the legend indicates for both data sets. (f) S_E vs T , where the tilted dashed lines indicate the logarithmic scaling $S_E = a \ln(\beta) + b$, where the slopes a seen for the TLH are similar to that for the SLH (SC6 data). The vertical dashed line labels the low-temperature scale $T_l \sim 0.2$ for TLH and the only temperature scale $T_s \sim 0.6$ for SLH. SC6 $\times 12$ stands for a $W = 6, L = 12$ square cylinder, and S_E scaling in the Heisenberg chain (length $L = 200$) is also plotted as a comparison.

can still recognize an enhanced intensity $S(M)$, which fades out eventually when T is decreased below T_l in Fig. 3(d). A quantitative comparison is given in Fig. 3(e).

From Fig. 3(e), we observe that $S(K)$ increases monotonously as T decreases. It is featureless around T_h , and eventually saturates at the lowest T due to finite system size. For $T > T_l$, $S(K)$ increases only slowly with decreasing temperature, and is independent of length L . It therefore shows no signature of incipient order there. For $T < T_l$, $S(K)$ rapidly increases, which eventually saturates with decreasing T in an L -dependent manner, due to finite-size effects.

Furthermore, we observe from Fig. 3(e) that $S(M)$ develops a well-pronounced maximum around T_h . The maximum is already stable with system size, hence can be considered a feature in the thermodynamic limit. This is consistent with a picture that RLEs are activated near the M points.

MPO entanglement. The two-energy-scale scenario also leaves a characteristic trace in the entanglement entropy S_E , computed at a bond (near the center) of the MPO [20, 58, 59].

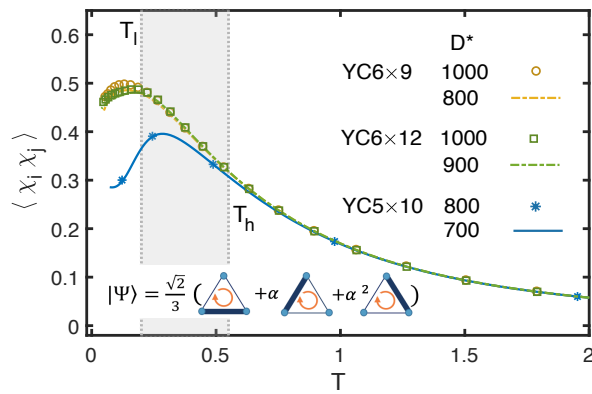


FIG. 4. (Color online) Chiral correlations on cylinders, YC5 and YC6 (for YC4, see Ref. [21]). The inset represents the eigenstates Ψ (and Ψ^*) of the chiral operator χ (Fig. 1) with non-zero eigenvalues $\pm\sqrt{12}$. They have total spin $S = 1/2$, and hence are superpositions of configurations with two-site singlet dimers (thick lines) whose spins are fixed in clockwise order (arrow). Having $\alpha = \exp(2\pi i/3)$, this demonstrates the chiral nature.

Gapless low-energy excitations in 1+1D conformal field theory (CFT) can give rise to a logarithmic increase of the entanglement, $S_E \propto -\frac{c}{3} \ln T$ with c the conformal central charge [20, 60, 61]. One can also observe logarithmic S_E behavior in the 2D SLH model, related to the spontaneous SU(2) symmetry breaking (at $T = 0$) [20], as also added for reference (“SC6” data) in Fig. 3(f).

We find similar behavior of the S_E profiles of the TLH on YC5 and YC6 geometries in Fig. 3(f) down to $T = 0.04$, with bond dimension $D^* \lesssim 1000$ multiplets ($D \sim 4D^*$ states). Interestingly, the lower-energy scale $T_l \sim 0.2$ (vertical dashed line) signals the onset of logarithmic entanglement scaling versus T , which in agreement with Fig. 2(a) already coincides for $W = 5$ and 6. For YC5, the window with logarithmic entanglement is rather narrow, below of which S_E saturates as we already approach the ground state. For YC6, the entanglement continues to increase down to our lowest temperature $T = 0.03$. We associate the logarithmic S_E behavior with the onset of incipient order, which is closely related to SU(2) symmetry breaking at $T = 0$ that gives rise, e.g., to a $1/(N = LW)$ level spacing in the low-energy tower of states [2]. Concomitantly, we also observe a qualitative change of behaviors in the entanglement spectra at T_l [21].

Scalar chiral correlations. Chiral correlations in the TLH have raised great interest since the proposal of a Kalmeyer-Laughlin chiral spin liquid [62]. Intriguingly, recent $T = 0$ studies on the fermionic triangular lattice Hubbard model proposed a chiral intermediate phase versus Coulomb repulsion which thus breaks time reversal symmetry [63]. While debated [64], we take this as a strong motivation to also study traces of chiral correlations in the TLH at finite T .

In Fig. 4, we present the chiral correlation $\langle \chi_i \chi_j \rangle$ between two nearest-triangles i, j in the system center, as defined with Fig. 1. This shows that chiral correlations are weak in both high- and low-temperature limit, while they become strong

[63] in the intermediate temperature regime, with a peak around T_l . Below T_l , the chiral correlations drop strongly, giving way to the buildup of coplanar incipient order.

Discussion. Our study suggests a tight connection between RLEs and chiral correlations in the intermediate regime $T_l \lesssim T \lesssim T_h$ (cf. Fig. 4). In this sense, we speculate that RLEs activated in the intermediate-temperature regime indicate phase-coherent rotating dimers, as schematically sketched with Fig. 4. Given that the complex phase of the dimers “rotates” by 2π , this suggests a possible link to a topological, vortexlike nature of the RLEs. Moreover, it resembles Feynman’s notion of rotons in terms of quantized vortices in He⁴ [42] via an exact mapping of TLH to a system of hardcore bosons. The latter further underlines the striking analogy between the anomalous thermodynamics of the TLH and the renowned roton thermodynamics in He⁴ [65, 66].

The low-energy scale T_l can be tuned by deforming the Hamiltonian, e.g., by altering the level of frustration by adding a next-nearest J_2 coupling to the TLH. We see that increasing J_2 reduces T_l , as well as the height of the corresponding peak in the specific heat, suggesting that the RLE gap is decreasing and the influence can thus spread down to even lower-temperature/energy scales, in consistency with dynamical studies of the J_1 - J_2 TLH [67, 68]. In addition, TLH can be continuously deformed into the SLH, where T_l increases and eventually merges with T_h once sufficiently close to the SLH. We refer more details to the Supplemental Materials [21].

Outlook. A detailed study of the microscopic nature of RLEs, e.g., via dynamical correlations at finite temperature, is beyond the scope of the present paper, and is thus left for future research. Further stimulating insights and possible superfluid analogies are also expected from an analysis of the interplay of external magnetic fields and thermal fluctuations in TLH [69, 70] with clear experimental relevance [37].

Acknowledgments. WL and LC would like to thank Yi Cui and Wei-Qiang Yu for providing their original data of Ba₈CoNb₆O₂₄. WL is indebted to Lei Wang, Zi Cai, Hong-Hao Tu, Zheng-Xin Liu, Xue-Feng Zhang, Bruce Normand, and Jie Ma for stimulating discussions. This work was supported by the National Natural Science Foundation of China (Grant No. 11504014, 11834014, and 11874078) and supported by the Deutsche Forschungsgemeinschaft (DFG, German Research Foundation) under Germany’s Excellence Strategy – EXC-2111 – 390814868. B.-B.C. was supported by the German Research foundation, DFG WE4819/3-1. A.W. was funded by DFG WE4819/2-1 and DOE DE-SC0012704 without temporal overlap. W.L. and S.-S.G. were supported by the Fundamental Research Funds for the Central Universities.

* weichselbaum@bnl.gov

† w.li@buaa.edu.cn

[1] P. W. Anderson, “Resonating valence bonds: A new kind of

- insulator?” *Mater. Res. Bull.* **8**, 153 (1973).
- [2] B. Bernu, C. Lhuillier, and L. Pierre, “Signature of Néel order in exact spectra of quantum antiferromagnets on finite lattices,” *Phys. Rev. Lett.* **69**, 2590 (1992).
- [3] L. Capriotti, A. E. Trumper, and S. Sorella, “Long-range Néel order in the triangular Heisenberg model,” *Phys. Rev. Lett.* **82**, 3899 (1999).
- [4] S. R. White and A. L. Chernyshev, “Néel order in square and triangular lattice Heisenberg models,” *Phys. Rev. Lett.* **99**, 127004 (2007).
- [5] N. Elstner, R. R. P. Singh, and A. P. Young, “Finite temperature properties of the spin-1/2 Heisenberg antiferromagnet on the triangular lattice,” *Phys. Rev. Lett.* **71**, 1629 (1993).
- [6] N. Elstner, R. R. P. Singh, and A. P. Young, “Spin-1/2 Heisenberg antiferromagnet on the square and triangular lattices: A comparison of finite temperature properties,” *J. Appl. Phys.* **75**, 5943 (1994).
- [7] S. A. Kulagin, N. Prokof’ev, O. A. Starykh, B. Svistunov, and C. N. Varney, “Bold diagrammatic monte carlo method applied to fermionized frustrated spins,” *Phys. Rev. Lett.* **110**, 070601 (2013).
- [8] N. D. Mermin and H. Wagner, “Absence of ferromagnetism or antiferromagnetism in one- or two-dimensional isotropic Heisenberg models,” *Phys. Rev. Lett.* **17**, 1133 (1966).
- [9] S. Chakravarty, B. I. Halperin, and D. R. Nelson, “Low-temperature behavior of two-dimensional quantum antiferromagnets,” *Phys. Rev. Lett.* **60**, 1057 (1988).
- [10] S. Chakravarty, B. I. Halperin, and D. R. Nelson, “Two-dimensional quantum Heisenberg antiferromagnet at low temperatures,” *Phys. Rev. B* **39**, 2344 (1989).
- [11] B. B. Beard, R. J. Birgeneau, M. Greven, and U.-J. Wiese, “Square-lattice Heisenberg antiferromagnet at very large correlation lengths,” *Phys. Rev. Lett.* **80**, 1742 (1998).
- [12] J.-K. Kim and M. Troyer, “Low temperature behavior and crossovers of the square lattice quantum Heisenberg antiferromagnet,” *Phys. Rev. Lett.* **80**, 2705 (1998).
- [13] N. Elstner, A. Sokol, R. R. P. Singh, M. Greven, and R. J. Birgeneau, “Spin dependence of correlations in two-dimensional square-lattice quantum Heisenberg antiferromagnets,” *Phys. Rev. Lett.* **75**, 938 (1995).
- [14] M. Greven, R. J. Birgeneau, Y. Endoh, M. A. Kastner, B. Keimer, M. Matsuda, G. Shirane, and T. R. Thurston, “Spin correlations in the 2D Heisenberg antiferromagnet $\text{Sr}_2\text{CuO}_2\text{Cl}_2$: Neutron scattering, monte carlo simulation, and theory,” *Phys. Rev. Lett.* **72**, 1096 (1994).
- [15] R. R. P. Singh and D. A. Huse, “Microscopic calculation of the spin-stiffness constant for the spin-1/2 square-lattice Heisenberg antiferromagnet,” *Phys. Rev. B* **40**, 7247 (1989).
- [16] W. Zheng, J. O. Fjærestad, R. R. P. Singh, R. H. McKenzie, and R. Coldea, “Excitation spectra of the spin- $\frac{1}{2}$ triangular-lattice Heisenberg antiferromagnet,” *Phys. Rev. B* **74**, 224420 (2006).
- [17] P. Azaria, B. Delamotte, and D. Mouhanna, “Low-temperature properties of two-dimensional frustrated quantum antiferromagnets,” *Phys. Rev. Lett.* **68**, 1762 (1992).
- [18] W. Li, S.-J. Ran, S.-S. Gong, Y. Zhao, B. Xi, F. Ye, and G. Su, “Linearized tensor renormalization group algorithm for the calculation of thermodynamic properties of quantum lattice models,” *Phys. Rev. Lett.* **106**, 127202 (2011).
- [19] B.-B. Chen, Y.-J. Liu, Z. Chen, and W. Li, “Series-expansion thermal tensor network approach for quantum lattice models,” *Phys. Rev. B* **95**, 161104(R) (2017).
- [20] B.-B. Chen, L. Chen, Z. Chen, W. Li, and A. Weichselbaum, “Exponential thermal tensor network approach for quantum lattice models,” *Phys. Rev. X* **8**, 031082 (2018).
- [21] See Supplemental Material for more details of the thermal tensor network methods including the XTRG and TPO approaches (Sec. I), for thermal data on XC4 and XC6, including internal energy versus T , dependence of the low-temperature scale T_l on length L , entanglement spectroscopy, correlation length ξ vs T , as well as finite- T chiral correlations on YC4 (Sec. II), and for thermodynamics of the J_1 - J_2 TLH and frustrated SLH models (Sec. III), which include Refs. [22–35].
- [22] A. Weichselbaum, “Non-abelian symmetries in tensor networks: A quantum symmetry space approach,” *Ann. Phys.* **327**, 2972 (2012).
- [23] L. De Lathauwer, B. De Moor, and J. Vandewalle, “A multilinear singular value decomposition,” *SIAM Journal on Matrix Analysis and Applications* **21**, 1253 (2000).
- [24] Z. Y. Xie, J. Chen, J. F. Yu, X. Kong, B. Normand, and T. Xiang, “Tensor renormalization of quantum many-body systems using projected entangled simplex states,” *Phys. Rev. X* **4**, 011025 (2014).
- [25] H. C. Jiang, Z. Y. Weng, and T. Xiang, “Accurate determination of tensor network state of quantum lattice models in two dimensions,” *Phys. Rev. Lett.* **101**, 090603 (2008).
- [26] W. Li, J. von Delft, and T. Xiang, “Efficient simulation of infinite tree tensor network states on the Bethe lattice,” *Phys. Rev. B* **86**, 195137 (2012).
- [27] J. Jordan, R. Orús, G. Vidal, F. Verstraete, and J. I. Cirac, “Classical simulation of infinite-size quantum lattice systems in two spatial dimensions,” *Phys. Rev. Lett.* **101**, 250602 (2008).
- [28] A. Weichselbaum and S. R. White, “Incommensurate correlations in the anisotropic triangular Heisenberg lattice,” *Phys. Rev. B* **84**, 245130 (2011).
- [29] Th. Jolicoeur and J. C. Le Guillou, “Spin-wave results for the triangular Heisenberg antiferromagnet,” *Phys. Rev. B* **40**, 2727 (1989).
- [30] A. V. Chubukov, T. Senthil, and S. Sachdev, “Universal magnetic properties of frustrated quantum antiferromagnets in two dimensions,” *Phys. Rev. Lett.* **72**, 2089 (1994).
- [31] Z. Zhu and S. R. White, “Spin liquid phase of the $S = \frac{1}{2}$ J_1 - J_2 Heisenberg model on the triangular lattice,” *Phys. Rev. B* **92**, 041105(R) (2015).
- [32] W.-J. Hu, S.-S. Gong, W. Zhu, and D. N. Sheng, “Competing spin-liquid states in the spin- $\frac{1}{2}$ Heisenberg model on the triangular lattice,” *Phys. Rev. B* **92**, 140403(R) (2015).
- [33] Y. Iqbal, W.-J. Hu, R. Thomale, D. Poilblanc, and F. Becca, “Spin liquid nature in the Heisenberg J_1 - J_2 triangular antiferromagnet,” *Phys. Rev. B* **93**, 144411 (2016).
- [34] S.-S. Gong, W. Zhu, J.-X. Zhu, D. N. Sheng, and K. Yang, “Global phase diagram and quantum spin liquids in a spin- $\frac{1}{2}$ triangular antiferromagnet,” *Phys. Rev. B* **96**, 075116 (2017).
- [35] E. Manousakis, “The spin-1/2 Heisenberg antiferromagnet on a square lattice and its application to the cuprous oxides,” *Rev. Mod. Phys.* **63**, 1 (1991).
- [36] R. Rawl, L. Ge, H. Agrawal, Y. Kamiya, C. R. Dela Cruz, N. P. Butch, X. F. Sun, M. Lee, E. S. Choi, J. Oitmaa, C. D. Batista, M. Mourigal, H. D. Zhou, and J. Ma, “ $\text{Ba}_3\text{CoSb}_2\text{O}_9$: A spin- $\frac{1}{2}$ triangular-lattice Heisenberg antiferromagnet in the two-dimensional limit,” *Phys. Rev. B* **95**, 060412(R) (2017).
- [37] Y. Cui, J. Dai, P. Zhou, P. S. Wang, T. R. Li, W. H. Song, J. C. Wang, L. Ma, Z. Zhang, S. Y. Li, G. M. Luke, B. Normand, T. Xiang, and W. Yu, “Mermin-Wagner physics, (H , T) phase diagram, and candidate quantum spin-liquid phase in the spin- $\frac{1}{2}$ triangular-lattice antiferromagnet $\text{Ba}_8\text{CoNb}_6\text{O}_{24}$,” *Phys. Rev. Materials* **2**, 044403 (2018).
- [38] A. Mezio, L O Manuel, R R P Singh, and A E Trumper, “Low temperature properties of the triangular-lattice antiferromagnet:

- a bosonic spinon theory,” *New J. Phys.* **14**, 123033 (2012).
- [39] A. Mezio, C. N. Sposetti, L. O. Manuel, and A. E. Trumper, “A test of the bosonic spinon theory for the triangular antiferromagnet spectrum,” *EPL (Europhysics Letters)* **94**, 47001 (2011).
- [40] W. Zheng, John O. Fjærestad, R. R. P. Singh, R. H. McKenzie, and Radu Coldea, “Anomalous excitation spectra of frustrated quantum antiferromagnets,” *Phys. Rev. Lett.* **96**, 057201 (2006).
- [41] O. A. Starykh, A. V. Chubukov, and A. G. Abanov, “Flat spin-wave dispersion in a triangular antiferromagnet,” *Phys. Rev. B* **74**, 180403(R) (2006).
- [42] R. P. Feynman, “Atomic theory of the two-fluid model of liquid helium,” *Phys. Rev.* **94**, 262–277 (1954).
- [43] J. Ma, Y. Kamiya, Tao Hong, H. B. Cao, G. Ehlers, W. Tian, C. D. Batista, Z. L. Dun, H. D. Zhou, and M. Matsuda, “Static and dynamical properties of the spin-1/2 equilateral triangular-lattice antiferromagnet $\text{Ba}_3\text{CoSb}_2\text{O}_9$,” *Phys. Rev. Lett.* **116**, 087201 (2016).
- [44] S. Ito, N. Kurita, H. Tanaka, S. Ohira-Kawamura, K. Nakajima, S. Itoh, K. Kuwahara, and K. Kakurai, “Structure of the magnetic excitations in the spin-1/2 triangular-lattice Heisenberg antiferromagnet $\text{Ba}_3\text{CoSb}_2\text{O}_9$,” *Nature Commun.* **8**, 235 (2017).
- [45] A. L. Chernyshev and M. E. Zhitomirsky, “Magnon decay in noncollinear quantum antiferromagnets,” *Phys. Rev. Lett.* **97**, 207202 (2006).
- [46] A. L. Chernyshev and M. E. Zhitomirsky, “Spin waves in a triangular lattice antiferromagnet: Decays, spectrum renormalization, and singularities,” *Phys. Rev. B* **79**, 144416 (2009).
- [47] M. Mourigal, W. T. Fuhrman, A. L. Chernyshev, and M. E. Zhitomirsky, “Dynamical structure factor of the triangular-lattice antiferromagnet,” *Phys. Rev. B* **88**, 094407 (2013).
- [48] C. Luo, T. Datta, Z. Huang, and D.-X. Yao, “Signatures of indirect K -edge resonant inelastic X-ray scattering on magnetic excitations in a triangular-lattice antiferromagnet,” *Phys. Rev. B* **92**, 035109 (2015).
- [49] J. Alicea, O. I. Motrunich, and M. P. A. Fisher, “Theory of the algebraic vortex liquid in an anisotropic spin- $\frac{1}{2}$ triangular antiferromagnet,” *Phys. Rev. B* **73**, 174430 (2006).
- [50] H. Kawamura, A. Yamamoto, and T. Okubo, “ Z_2 -vortex ordering of the triangular-lattice Heisenberg antiferromagnet,” *J. Phys. Soc. Jpn.* **79**, 023701 (2010).
- [51] M. V. Gvozdkova, P. E. Melchy, and M. E. Zhitomirsky, “Magnetic phase diagrams of classical triangular and kagome antiferromagnets,” *J. Phys. Condens. Matter.* **23**, 164209 (2011).
- [52] L. Seabra, T. Momoi, P. Sindzingre, and N. Shannon, “Phase diagram of the classical Heisenberg antiferromagnet on a triangular lattice in an applied magnetic field,” *Phys. Rev. B* **84**, 214418 (2011).
- [53] I. S. Popov, P. V. Prudnikov, A. N. Ignatenko, and A. A. Katanin, “Universal berezinskii-kosterlitz-thouless dynamic scaling in the intermediate time range in frustrated heisenberg antiferromagnets on a triangular lattice,” *Phys. Rev. B* **95**, 134437 (2017).
- [54] B. Dalla Piazza, M. Mourigal, N. B. Christensen, G. J. Nilsen, P. Tregenna-Piggott, T. G. Perring, M. Enderle, D. F. McMorrow, D. A. Ivanov, and H. M. Rønnow, “Fractional excitations in the square-lattice quantum antiferromagnet,” *Nat. Phys.* **11**, 62 (2014).
- [55] R. Verresen, F. Pollmann, and R. Moessner, “Quantum dynamics of the square-lattice Heisenberg model,” *Phys. Rev. B* **98**, 155102 (2018).
- [56] R. Verresen, F. Pollmann, and R. Moessner, “Strong quantum interactions prevent quasiparticle decay,” *ArXiv e-prints* (2018), arXiv:1810.01422 [cond-mat.str-el].
- [57] E. A. Ghioldi, M. G. Gonzalez, S.-S. Zhang, Y. Kamiya, L. O. Manuel, A. E. Trumper, and C. D. Batista, “Dynamical structure factor of the triangular antiferromagnet: Schwinger boson theory beyond mean field,” *Phys. Rev. B* **98**, 184403 (2018).
- [58] F. Verstraete, J. J. García-Ripoll, and J. I. Cirac, “Matrix product density operators: Simulation of finite-temperature and dissipative systems,” *Phys. Rev. Lett.* **93**, 207204 (2004).
- [59] A. E. Feiguin and S. R. White, “Finite-temperature density matrix renormalization using an enlarged Hilbert space,” *Phys. Rev. B* **72**, 220401(R) (2005).
- [60] T. Barthel, “One-dimensional quantum systems at finite temperatures can be simulated efficiently on classical computers,” *arXiv:1708.09349*.
- [61] J. Dubail, “Entanglement scaling of operators: a conformal field theory approach, with a glimpse of simulability of long-time dynamics in $1 + 1D$,” *J. Phys. A: Math. Theor.* **50**, 234001 (2017).
- [62] V. Kalmeyer and R. B. Laughlin, “Equivalence of the resonating-valence-bond and fractional quantum Hall states,” *Phys. Rev. Lett.* **59**, 2095 (1987).
- [63] A. Szasz, J. Motruk, M. P. Zaletel, and J. E. Moore, “Observation of a chiral spin liquid phase of the Hubbard model on the triangular lattice: a density matrix renormalization group study,” *ArXiv e-prints* (2018), arXiv:1808.00463.
- [64] T. Shirakawa, T. Tohyama, J. Kokalj, S. Sota, and S. Yunoki, “Ground-state phase diagram of the triangular lattice Hubbard model by the density-matrix renormalization group method,” *Phys. Rev. B* **96**, 205130 (2017).
- [65] J. D. Wasscher, H. C. Kramers, and C.J. Gorter, “The specific heat of liquid Helium between 0.25 and 1.9 K,” *Physica* **18**, 329 (1952).
- [66] P. J. Bendt, R. D. Cowan, and J. L. Yarnell, “Excitations in liquid helium: Thermodynamic calculations,” *Phys. Rev.* **113**, 1386–1395 (1959).
- [67] E. A. Ghioldi, A. Mezio, L. O. Manuel, R. R. P. Singh, J. Oitmaa, and A. E. Trumper, “Magnons and excitation continuum in XXZ triangular antiferromagnetic model: Application to $\text{Ba}_3\text{CoSb}_2\text{O}_9$,” *Phys. Rev. B* **91**, 134423 (2015).
- [68] F. Ferrari and F. Becca, “Dynamical structure factor of the J_1 - J_2 Heisenberg model on the triangular lattice: magnons, spinons, and gauge fields,” *ArXiv e-prints* (2019), arXiv:1903.05691.
- [69] C. Griset, S. Head, J. Alicea, and O. A. Starykh, “Deformed triangular lattice antiferromagnets in a magnetic field: Role of spatial anisotropy and Dzyaloshinskii-Moriya interactions,” *Phys. Rev. B* **84**, 245108 (2011).
- [70] O. A. Starykh, “Unusual ordered phases of highly frustrated magnets: a review,” *Rep. Prog. Phys.* **78**, 052502 (2015).

Supplemental Materials: Two-Temperature Scales in the Triangular-Lattice Heisenberg Antiferromagnet

FINITE-TEMPERATURE RENORMALIZATION GROUP APPROACHES

In this section, we recapitulate the two thermal tensor network approaches employed in the present study, i.e., the exponential tensor renormalization group (XTRG) based on matrix product operators (MPOs) and the tensor product operator (TPO) approach. The former is highly controllable while restricted to finite-size systems; the latter can be applied directly in the thermodynamic limit, but is constrained by finite bond dimensions as well as an approximate optimization scheme. Nevertheless, we exploit a combination of 1D/2D tensor network RG approaches to study the triangular lattice Heisenberg (TLH) model, and find the results of the two methods consistent.

Exponential Tensor Renormalization Group: A matrix product operator approach

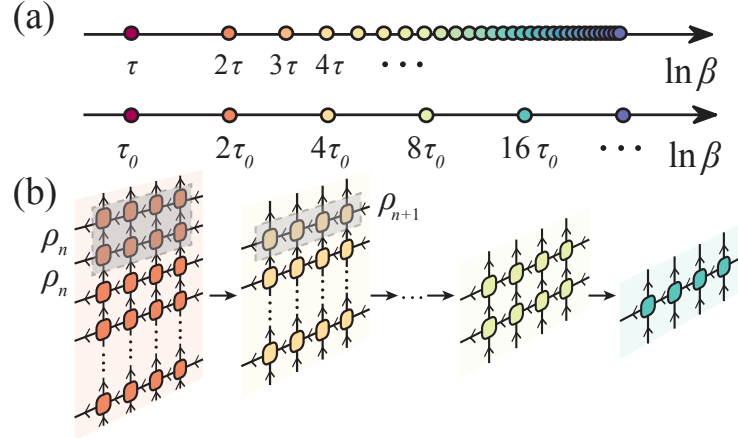


FIG. S1. (Color online) (a) Exponential vs. linear thermal evolution of the unnormalized density operator, $\rho \equiv e^{-\beta H}$. (b) The procedure of MPO doubling in XTRG, i.e. $\rho_{n+1} = \rho_n * \rho_n$ corresponding to $\beta_{n+1} = 2\beta_n = 2^n \tau_0$.

We start from the MPO-based XTRG approach, which was proposed in Ref. [20]. There the (unnormalized) thermal mixed state $\rho(\beta) \equiv e^{-\beta H}$ of the system is represented as 1D MPO, as depicted in Fig. S1(b). In the purification framework, $\rho(\beta)$ represents a thermo-double field, where the trace with its conjugate results in the partition function at 2β , i.e.,

$$Z(2\beta) = \text{Tr}[\rho(\beta) \cdot \rho^\dagger(\beta)]. \quad (\text{S1})$$

Similarly, one can compute thermodynamic quantities. While equivalent to the concept of purification, we emphasize, however, that here we always describe the density matrix as an MPO and thus as an operator. The added benefit of using $\rho\rho^\dagger$ as in Eq. (S1) is that it always yields a positive and, thus, a physical thermal density operator at inverse temperature 2β .

The evolution of $\rho(\beta)$ always starts from infinite temperature in thermal RG approaches, where the density operator is just a trivial identity, i.e. $\rho(0) = \mathbb{I}$. Conventional linear RG approaches evolve the density matrix linearly in β , i.e.,

$$\rho(n\tau) = \underbrace{\rho(\tau) \cdot \rho(\tau) \cdot \dots \cdot \rho(\tau)}_n \cdot I, \quad (\text{S2})$$

where τ is a small imaginary time (inverse temperature) step size that applies to all $\beta_{n+1} = \beta_n + \tau$. We refer to such a scheme, schematically depicted in the upper row of Fig. S1(a), as a linear thermal RG, see Ref. [18].

A recent insight from the logarithmic entanglement scaling in conformal field theory proves that the block-entanglement growth in a thermal MPO is upper bounded by $S_E \leq a \ln \beta + b$ with some constants a and b [60, 61]. This shows that the

entanglement entropy S_E of the MPO actually changes significantly only when β changes by a factor. In light of this, the linear evolution is realized to be a very slow cooling procedure, while a more efficient way is to follow the logarithmic temperature scale. A particularly simple and convenient choice is $\beta \rightarrow 2\beta$, i.e.,

$$\rho_{n+1} = \rho_n * \rho_n, \quad (\text{S3})$$

with $\rho_n \equiv \rho(2^n \tau_0)$, and τ_0 an arbitrarily small *initial* starting point. The asterisk here is a reminder to emphasize the underlying MPO product structure. This exponential procedure is illustrated in lower row of Fig. S1(a), as well as in Fig. S1(b), which reveal manifestly the efficiency of XTRG, i.e., the system reaches the lowest temperature exponentially fast. Similarly, by its very construction, XTRG can also start from an arbitrarily small τ_0 , which thus allows one to resort to a very simple but accurate initialization of ρ_0 , e.g. using series expansion,

$$\rho_0 \equiv \rho(\tau_0) = \sum_{n=0}^{n_c} \frac{(-\tau_0)^n}{n!} H^n, \quad (\text{S4})$$

even using a cutoff as small as $n_c = 1$ where the MPO for ρ_0 is given – up to a very minor adaptation – by the MPO of H itself with the *same* bond dimension. For comparison, $n_c = 2$ only includes one further doubling of the MPO of H with itself, an elementary MPO procedure in XTRG in any case. Overall, the techniques required to perform the expansion in Eq. (S4) have been developed in Ref. [19], dubbed as series-expansion thermal tensor network (SETTN) method.

Naively, one might expect that the numerical cost for the step in Eq. (S3) scales like $\mathcal{O}(D^6)$ with D the bond dimension of MPO, and thus represents a (prohibitively) expensive calculation. The numerical cost, however, can be strongly reduced to $\mathcal{O}(D^4)$ by resorting to a variational procedure (see [19] for details), thus allowing larger D in the calculation. In addition, thanks to the versatile QSpace framework [22], we have fully implemented non-Abelian symmetries in our XTRG simulations which effectively reduces the bond dimension by switching from D states to D^* multiplets. Conversely, for the case of SU(2) in the present study, we can therefore keep up to $D \lesssim 4 \times D^*$ individual U(1) states.

Finally, we would like to emphasize that XTRG is not only superior to conventional linear RG in efficiency, but also in terms of accuracy. Since the lowest temperature can be reached in an extremely speedy fashion, this results in a significantly smaller number of numerical iterations. Hence also the truncation error accumulation is greatly reduced. A detailed comparison of accuracies and efficiencies between XTRG and LTRG, as well as SETTN, also can be found in Ref. [20].

Tensor Product Operator Approach

As an alternative approach in our simulations, we also utilize the tensor product operator (TPO) approach, whose results generally are in agreement with XTRG. Here we provide details of our TPO algorithm together with more benchmark calculations. For practical and historical reasons, we still use a numerical code that is based on a linearized scheme in the imaginary time evolution based on Trotter decomposition in our TPO algorithm, and also does not yet exploit any symmetries. Its concepts, nevertheless, can equally well be generalized in the spirit of doubling of the density matrix as in XTRG.

TPO Representation of the Density Matrix

From a numerical efficiency point of view, it is favorable to describe the thermal states of TLH via an effective hexagonal lattice TN, as shown in Fig. S2. Furthermore, given that the TLH carries a 120° magnetic order at zero temperature, this naturally divides the sites on the TLH into three sublattices, which is also required for a Trotter decomposition in any case. Therefore we introduce three types of T tensors, T_a , T_b , and T_c on the A -, B -, and C -sites (orange, green and blue solid triangles in Fig. S2, respectively). All of them are rank-5 tensors with 2 physical indices and 3 geometric ones. The T tensors are interconnected to form the hexagonal tensor network (TN) in Fig. S2 along the x -, y -, z -bonds via three types of rank-3 S tensors, S_a , S_b and S_c (orange, green and blue solid circles, respectively) with no physical indices of their own. The S tensors reside on three distinct up-triangles, dubbed as a -, b -, and c -triangles, corresponding to the three sublattices A , B , and C , respectively. They contain disconnected subsets of nearest-neighbor terms on the TLH which can be readily utilized for a Trotter decomposition [cf. Eq. (S6)]. In Fig. S2 we also indicate how to wrap up the TPO on an XC, i.e., by imposing periodic boundary condition (BC) along the vertical direction.

Throughout, we assume that the (starting) configuration of the S tensors is in the canonical form,

$$\sum_{i,j} (S_\alpha)_{ijk}^* (S_\alpha)_{ijk'} = (\lambda_k^\alpha)^2 \delta_{kk'}. \quad (\text{S5})$$

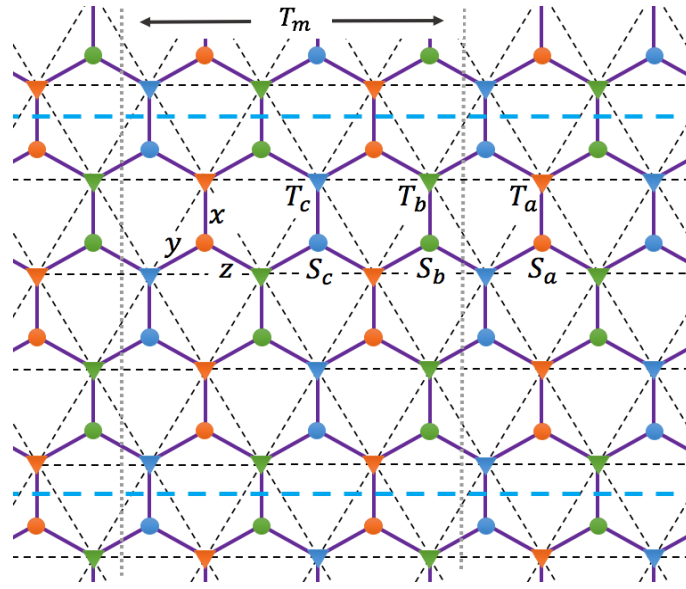


FIG. S2. (Color online) The triangular lattice (dashed lines) represented in the TPO ansatz (thick lines with symbols for tensors). Since we use Trotter decomposition within our TPO simulations, we need to differentiate sets of three tensors. There are three kinds of rank-5 tensors, i.e. tensors with five external indices, namely T_a , T_b and T_c (orange, green, and blue triangles, respectively) located on the sites of the TLH, where the two physical indices for bra and ket, i.e. σ and σ' , are omitted for simplicity. There are also three kinds of rank-3 intermediate tensors S_a , S_b and S_c (orange, green, and blue circles, respectively), without physical indices, residing in the center of the face of the up-triangles in the TLH. The geometrical bonds can be grouped by their orientation, labelled x , y and z . The two horizontal dashed blue lines denote the XC boundary condition, where the system is wrapped up vertically (having $W = 4$ in the plot above). The two vertical lines indicate the transfer matrix T_m along the cylinder where, by definition of a transfer matrix, all ‘internal’ indices, including the physical indices as well as intermediate geometric indices, should be traced, with the only open indices the thick lines crossing the vertical dashed lines.

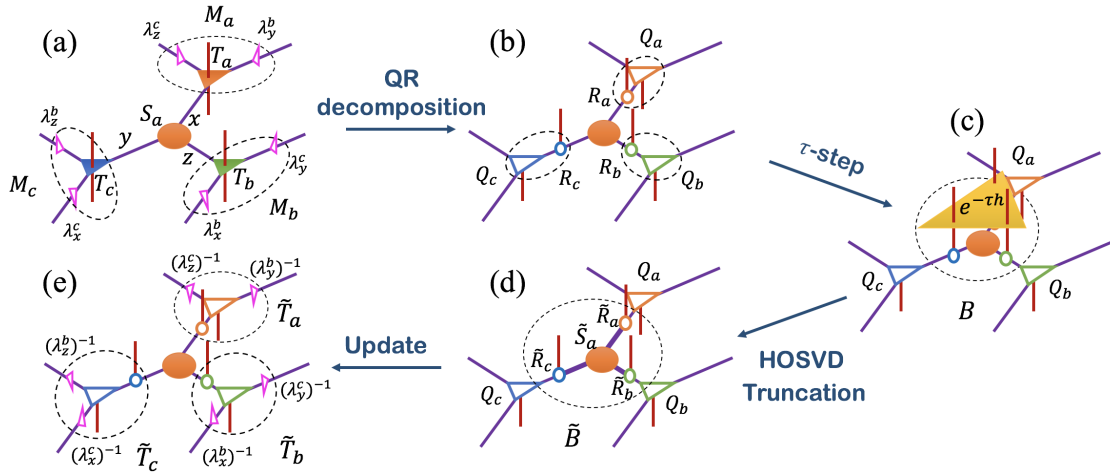


FIG. S3. (Color online) Procedure of a single projection step: (a) Absorptions of λ matrices, where the suggestive arrow with the λ 's indicates the (approximate) orthonormalization of the entire Bethe TNS. (b) QR decomposition, while also splitting off the upper physical indices. (c) Applying the triangular imaginary time step $e^{-\tau h}$ to the base tensor. (d) HOSVD of the base tensor. (e) truncate and update S_a as well as three T tensors.

where the $\alpha \in a, b, c$ labels different S tensors, and the bond indices (i, j, k) denotes cyclic permutations of (x, y, z) . This form can be achieved by higher-order singular-value decomposition (HOSVD), with a residual unitary out of the S tensors absorbed into the T tensors, and the singular values $\lambda_k^\alpha \geq 0$ reabsorbed into the S tensor. The contraction in Eq. (S5) thus regenerates a diagonal matrix with entries $(\lambda_k^\alpha)^2$. For a more detailed discussion of HOSVD, we refer the reader to Refs. [23, 24]

Imaginary-time Evolution and Simple Update Scheme of TPO

We utilize the Bethe-lattice approximation, also referred to as simple update [25, 26], in the imaginary-time evolution to optimize the TPO density matrix of the system from high to low temperatures. To be concrete, via a Trotter-Suzuki decomposition, the density matrix can be expressed as

$$\rho = e^{-\beta H} \approx (e^{-\tau H^A} e^{-\tau H^B} e^{-\tau H^C})^N \equiv (P^A P^B P^C)^N \quad \text{with} \quad P^\Lambda \equiv \prod_{i \in \Lambda} e^{-\tau h_i}, \quad (\text{S6})$$

where $H^\Lambda \equiv \sum_{i \in \Lambda} h_i$, with h_i the ‘triangular plaquette’ Hamiltonian on the up-triangle i in sublattice $\Lambda \in A, B, C$, and τ the Trotter step (chosen as $0.01 \sim 0.02$ in practice). By construction, $[h_i, h_{i'}] = 0$ for $i \neq i'$ within the same sublattice $i, i' \in \Lambda$. All of the h_i have identical form for the isotropic Heisenberg model considered here. We initialize with an infinite-temperature density matrix (direct product of identities), and apply the triangular operators P^Λ sequentially for $\Lambda \in A, B, C$. This is repeated iteratively to cool down the TPO density matrix.

To be specific, we now describe in detail the application of P^A , where the tensor S_a is surrounded by the tensors T_a, T_b and T_c (see Fig. S2 and also Fig. S3).

- (i) We firstly (re)generate the diagonal λ^α matrices as in Eq. (S5) out of the S_α tensors surrounding the T tensors, i.e. $\alpha \in \{b, c\}$.
- (ii) Next we absorb the λ 's into the T 's to construct the tensors M [Fig. S3(a)]

$$(M_a)_{xyz}^{\sigma'_a \sigma_a} = (T_a)_{xyz}^{\sigma'_a \sigma_a} \lambda_y^b \lambda_z^c, \quad (\text{S7a})$$

$$(M_b)_{xyz}^{\sigma'_b \sigma_b} = (T_b)_{xyz}^{\sigma'_b \sigma_b} \lambda_x^b \lambda_y^c, \quad (\text{S7b})$$

$$(M_c)_{xyz}^{\sigma'_c \sigma_c} = (T_c)_{xyz}^{\sigma'_c \sigma_c} \lambda_z^b \lambda_x^c \quad (\text{S7c})$$

(note that we explicitly indicate summation, i.e. there is no implicit summation here over double indices since the λ matrices are diagonal).

- (iii) Perform QR decompositions of M_a, M_b and M_c [Fig. S3(b)]

$$(M_a)_{x'yz}^{\sigma'_a \sigma_a} = \sum_x (Q_a)_{x'yz}^{\sigma'_a} (R_a)_{xx'}^{\sigma_a}, \quad (\text{S8a})$$

$$(M_b)_{xyz'}^{\sigma'_b \sigma_b} = \sum_z (Q_b)_{xyz'}^{\sigma'_b} (R_b)_{zz'}^{\sigma_b}, \quad (\text{S8b})$$

$$(M_c)_{xy'z}^{\sigma'_c \sigma_c} = \sum_y (Q_c)_{xy'z}^{\sigma'_c} (R_c)_{yy'}^{\sigma_c}. \quad (\text{S8c})$$

Here we have also split off the upper physical indices into the tensors R_a, R_b and R_c which significantly reduces the computational cost in the projection-truncation procedure in the next step.

- (iv) Construct the base tensor B by contracting R_a, R_b, R_c with S_a tensor

$$B_{xyz}^{\sigma_a \sigma_b \sigma_c} = \sum_{x', y', z'} (R_a)_{xx'}^{\sigma_a} (R_b)_{zz'}^{\sigma_b} (R_c)_{yy'}^{\sigma_c} (S_a)_{x'y'z'}, \quad (\text{S9a})$$

and apply the 3-site imaginary-time step $P = e^{-\tau h}$ onto the base tensor [Fig. S3(c)]

$$\tilde{B}_{xyz}^{\sigma_a \sigma_b \sigma_c} = \sum_{\sigma'_a, \sigma'_b, \sigma'_c} P_{\sigma'_a \sigma'_b \sigma'_c}^{\sigma_a \sigma_b \sigma_c} \cdot B_{xyz}^{\sigma'_a \sigma'_b \sigma'_c}. \quad (\text{S9b})$$

- (v) Take HOSVD of the modified base tensor \tilde{B} by performing independent SVD w.r.t. the index pairs (σ_a, x) , (σ_b, z) , and (σ_c, y) , providing the isometries \tilde{R}_a to \tilde{R}_c , respectively [Fig. S3(d)]. Then by projecting the original tensor \tilde{B} with $\tilde{P}_\alpha \equiv \tilde{R}_\alpha \tilde{R}_\alpha^\dagger$ on all three indices $\alpha \in \{a, b, c\}$, one obtains the updated tensor \tilde{S} ,

$$(\tilde{S}_a)_{xyz} = \sum_{\substack{\sigma_a \sigma_b \sigma_c \\ x' y' z'}} (\tilde{R}_a^*)_{x'x}^{\sigma_a} (\tilde{R}_b^*)_{z'z}^{\sigma_b} (\tilde{R}_c^*)_{y'y}^{\sigma_c} \tilde{B}_{x'y'z'}^{\sigma_a \sigma_b \sigma_c}, \quad (\text{S10a})$$

or equivalently,

$$\tilde{B}_{xyz}^{\sigma_a \sigma_b \sigma_c} = \sum_{x', y', z'} (\tilde{R}_a)_{xx'}^{\sigma_a} (\tilde{R}_b)_{zz'}^{\sigma_b} (\tilde{R}_c)_{yy'}^{\sigma_c} (\tilde{S}_a)_{x'y'z'}. \quad (\text{S10b})$$

In exact numerics, the bond dimensions of \tilde{S}_a would be generally enlarged by the local Hilbert space dimension d , and thus needs to be truncated. This is achieved by discarding the smallest singular values in λ , such that \tilde{P}_α becomes a true projector, namely to the sector of dominant singular values. The kept singular values are the ones that also occur in Eq. (S5). Without symmetry breaking, the three directions x, y, z are equivalent, and hence the S and T tensors may be chosen symmetric under cyclic permutation of these indices, throughout. This simplifies the TPO step above in that only a single SVD already suffices to obtain $\tilde{R} \equiv \tilde{R}_a = \tilde{R}_b = \tilde{R}_c$. In practice, the results were equivalent whether or not this lattice symmetry was enforced.

- (vi) The truncated \tilde{R} tensors in Eq. (S10b) can now be contracted (absorbed) into the Q tensors in (iii). By also undoing step (ii) by applying inverted λ^b and λ^c weights (note that in the above steps, only λ_ξ^a with $\xi \in \{x, y, z\}$ was altered, but the sets λ_ξ^b and λ_ξ^c remained the same), we obtain the updated \tilde{T} tensors [Fig. S3(e)],

$$(\tilde{T}_a)_{x'yz}^{\sigma'_a \sigma_a} = \sum_x (Q_a)_{xyz}^{\sigma'_a} (\tilde{R}_a)_{xx'}^{\sigma_a} / (\lambda_y^b \lambda_z^c), \quad (\text{S11a})$$

$$(\tilde{T}_b)_{xyz'}^{\sigma'_b \sigma_b} = \sum_z (Q_b)_{xyz}^{\sigma'_b} (\tilde{R}_b)_{zz'}^{\sigma_b} / (\lambda_x^b \lambda_y^c), \quad (\text{S11b})$$

$$(\tilde{T}_c)_{xy'z}^{\sigma'_c \sigma_c} = \sum_y (Q_c)_{xyz}^{\sigma'_c} (\tilde{R}_c)_{yy'}^{\sigma_c} / (\lambda_z^b \lambda_x^c). \quad (\text{S11c})$$

Evaluation of thermal quantities

The S and T tensors from the simple update above are inserted into the 2D-TN of Fig. S2. One then needs to contract this TN efficiently in the thermodynamic limit to obtain the partition function, and thus physical thermal properties such as free energy, energy, magnetization, etc. This constitutes another essential challenge of the algorithm. For finite-size cylinders with a small width W , e.g., XC4, we perform exact contractions; while for an infinite-size system, we use conventional boundary matrix product state (MPS) technique adopted in infinite projected entanglement pair state (iPEPS) algorithms [27].

For both the XC4 and infinite-size systems, the dominating eigenvector as well as eigenvalue of the horizontal transfer matrix T_m (i.e. with a cut in Y direction, see Fig. S2) can be obtained exactly (for the XC4) or approximately (for infinite systems) by iteratively contracting a trial initial vector with T_m until convergence. For this, double-layer TPO, i.e. using $\rho(\beta/2)^\dagger \rho(\beta/2) \rightarrow \rho(\beta)$ to enforce positivity, is orders of magnitude more expensive as compared to the relatively cheap single-layer formalism of TPO. For the XC4 system, the single-layer TPO computations are affordable at a cost of $O(D^6)$, where D up to 60 is the bond dimension of TPO. For the subsequent embedding into an infinite 2D TNS, the TPO cost scales as $O(\chi^3 D^3)$, with χ the bond dimension of the boundary MPS. In practice, we choose D up to 40 and $\chi \sim 4D$, which is affordable, yet also ensures data convergence over the parameter χ .

TRIANGULAR LATTICE ANTIFERROMAGNET

Benchmark results on XC4 geometry

In contrast to YC geometries which correspond to a cylinder with straight ends, the XC geometry results in a cylinder with zigzag ends [28]. Also note that the YC systems have a unique shortest distance path along the nearest-neighbor bonds of the TLH around the circumference when starting from an arbitrary but fixed lattice site. This can favor 1D RVB stripe structures around the circumference, in contrast to XC systems. Here therefore we apply both methods above to an XC4 geometry, i.e., of width $W = 4$, as shown in Fig. S4(a). For XTRG, we use our default aspect ratio $L/W = 2$, and map the 2D lattice into a 1D structure along the snake line also shown in Fig. S4(a). For the TPO method, we optimise the tensors T and S directly in the thermodynamic limit, and connect the local tensors on an infinitely long XC4 lattice.

In Fig. S4(b), the specific heat, c_V , of XC4 obtained by XTRG by retaining $D^* = 400$ multiplets, and by TPO with different bond dimensions D up to 60, is presented in comparison with HTSE. The two temperature scales are apparent in both cases, although the low temperature peak appears at $T_l^* \sim 0.28$ somewhat above the value 0.20 obtained on wider YC geometries. This

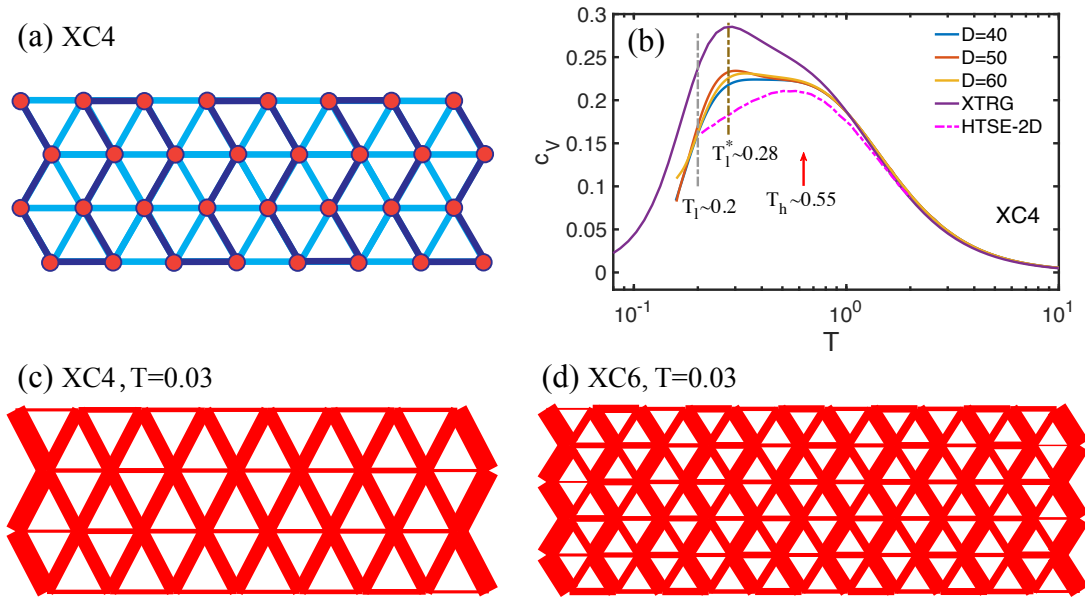


FIG. S4. (Color online) (a) XC geometry where the dark blue lines indicate the MPO path in the XTRG simulations. (b) Comparison of specific heat c_V between TPO and XTRG on XC4 and, for reference, also HTSE-2D, i.e., not constrained to the XC4 geometry. The high temperature scale, $T_h \sim 0.55$, indicates the high temperature round peak, while the low temperature scale, $T_l^* \sim 0.28$, is slightly higher than $T_l \sim 0.20$ for wider systems, e.g., YC6 in the main text as well as XC6 below. (c,d) illustrate the bond energy textures on XC4 (no vertical stripes) and XC6 (vertical stripes) geometries, consistent with $T = 0$ DMRG simulations [28]. The explicit symmetry breaking in the vertical direction by forming stripes, here in (d), at finite temperature is necessarily linked to the choice of the open boundary edges.

is due to strong finite-site effects on XC4, which will be further analyzed shortly by calculating the static structure factor $S(q)$. Another distinct feature is that the lower-temperature peaks in TPO curves are significantly lower than for the XTRG results. This may also hint a smaller finite-size effect in the TPO approach (due to its simple update scheme).

In Fig. S5(a-f), we visualize the static structure factors $S(q)$ for XC4 in the first BZ at various temperatures, which are marked by grey solid lines in Fig. S5(g) together with the corresponding panel reference [(a-d) from TPO, and (e,f) from XTRG calculations]. When lowering the temperature, the triangular lattice symmetry is broken around T_h due to the finite system size, as manifested by the slightly different behavior of the data for the otherwise equivalent points M_1 and M_2 [indicated by markers in Fig. S5(a)]. For temperatures below T_h , one can observe that $S(M_1)$, which points perpendicular to the direction of the cylinder, turns brighter whereas $S(M_2)$ and $S(M_3)$ start losing weight. This indicates a tendency for enhanced AF, i.e. Néel like correlations around the circumference of the cylinder. Note that for XC4 one has equivalent, i.e. non-symmetry broken shortest zig-zag paths around the circumference of the cylinder [vertical direction in Fig. S4(c)].

In Fig. S5(g) we also directly compare $S(q)$ vs. T at $M_{1,2}$ and K from both methods, XTRG as well as TPO. At the K and M_2 points, the data from the two methods coincide, while for M_1 , the XTRG data reaches the low- T limit faster. This may be attributed to a stronger (or cleaner) finite-size effect in XTRG, as compared to the TPO data which, despite being evaluated on a cylinder, originates from an infinite-system simple update. A similar conclusion was already drawn from the data in Fig. S4(b) regarding the higher c_V peak for XTRG at T_l^* .

Specific heat, susceptibility, and structure factor for cylinders up to $W = 6$

We present our XTRG results on XC6 and YC6 systems for the specific heat and static susceptibility in Fig. S6, and for the static structure factor in Fig. S7. Overall, we expect clearly reduced finite-size effects as compared to the width $W = 4$ systems.

The specific heat, c_V , on XC6, shown in Fig. S6(a), agrees well with both YC6 and HTSE in the high temperature regime, $T \gtrsim T_h$. The observed lower energy scale in this data is stable around $T_l \sim 0.2$ also for this wider system. In Fig. S6(b), we compare our XTRG data for the magnetic susceptibility, χ_0 vs. T , on XC6 with other results including two experimental measurements, XC4, YC5 and 6, HTSE, etc. A good agreement between XC6 data and experimental results can be observed, although YC6 produces χ_0 mostly close to experiments and constitutes the overall most suitable geometry.

From Figs. S6(a,b) we can conclude that although XC6 has many features in common with YC6, it suffers larger finite-size effects and is less favorable in approximating the thermodynamic limit. This can be directly seen in the bond energy texture

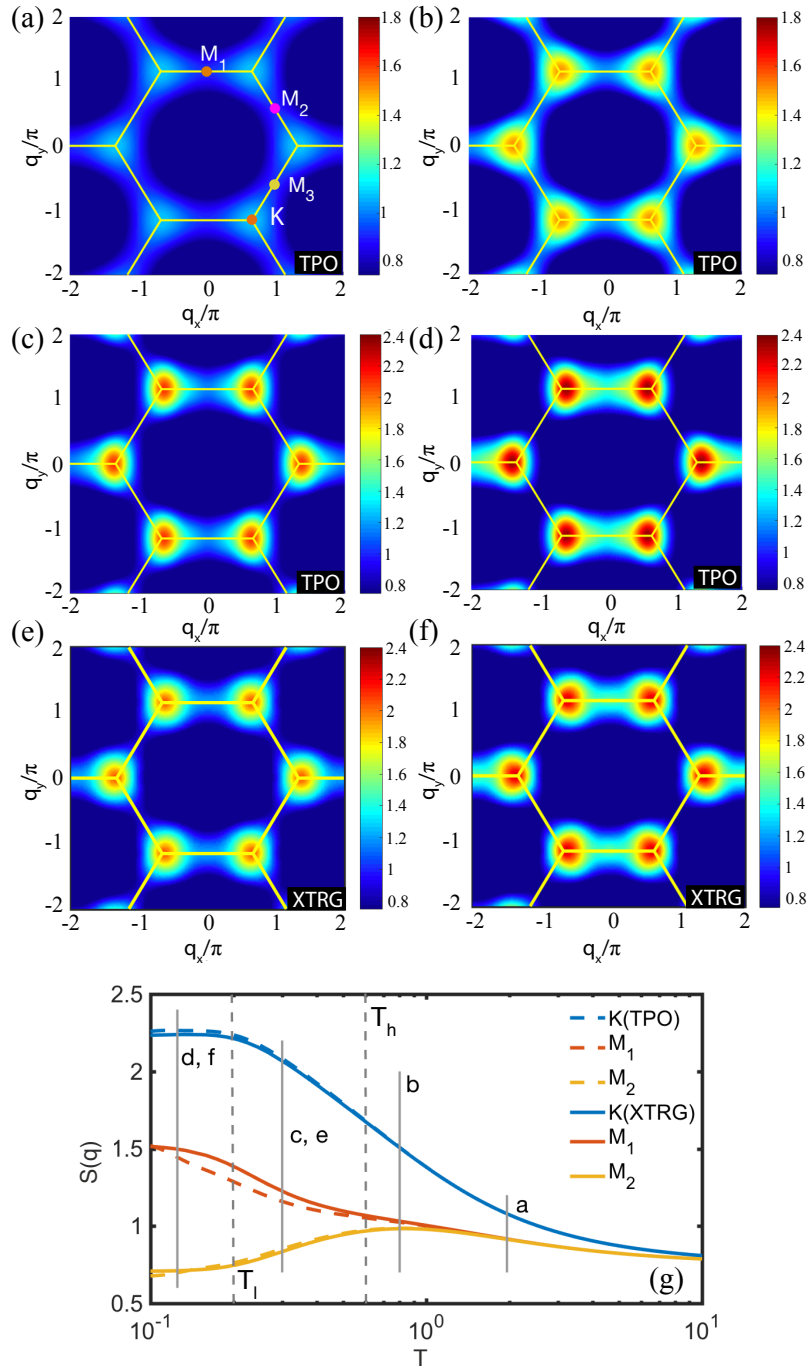


FIG. S5. (Color online) Static structure factor $S(q)$ of XC4, i.e., with q_x pointing along the cylinder, computed by TPO (a-d) and XTRG (e,f) at various temperatures, $T \simeq 2, 0.8, 0.3, 0.125$, as also indicated by the vertical solid gray lines in (g). While only having $W = 4$ discrete q_y momenta due to periodic BC, we interpolate by adding further intermediate points q_y in the Fourier transform in $S(q)$ to obtain for overall smoother results. The vertical dashed lines in (g) indicate T_l and T_h . Overall, the TPO data in (c,d) shows good agreement with the XTRG data in (e,f) at the same respective temperatures. (g) $S(q)$ at $q = K$ and two types of M points [cf. panel (a)] vs. T , again with good quantitative agreement between TPO and XTRG.

on XC6 in Fig. S4(d). Although being measured at a finite temperature, it is consistent with previous DMRG studies of the ground state properties [28], where spontaneous zig-zag stripe formation around the circumference of the cylinder is found for XC systems of width $2n + 4$, with n an integer.

The structure factor, $S(q)$, is analyzed in Fig. S7, where XC6 [Fig. S7(a)] is compared to YC6 [Fig. S7(b)]. By reaching temperatures as low as $T \sim 0.1 < T_l$, we expect signatures of incipient 120° order to be present in both systems. For YC6

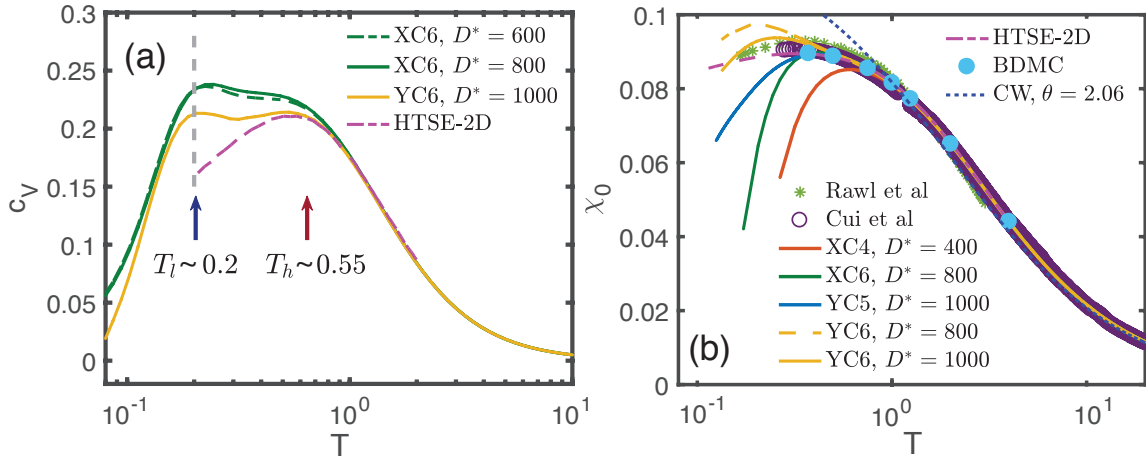


FIG. S6. (Color online) (a) Specific heat c_V on XC6 and YC6 lattices. (b) Static magnetic susceptibility χ_0 vs. T . We also added HTSE-2D data and other data from the literature for reference, as well as a simple Curie Weiss (CW) estimate (same as in Fig. 2 in the main paper). For a discussion of numerical cost, i.e. the growth of the block entanglement S_E with decreasing T , see, e.g., Fig. 3(f) in the main text.

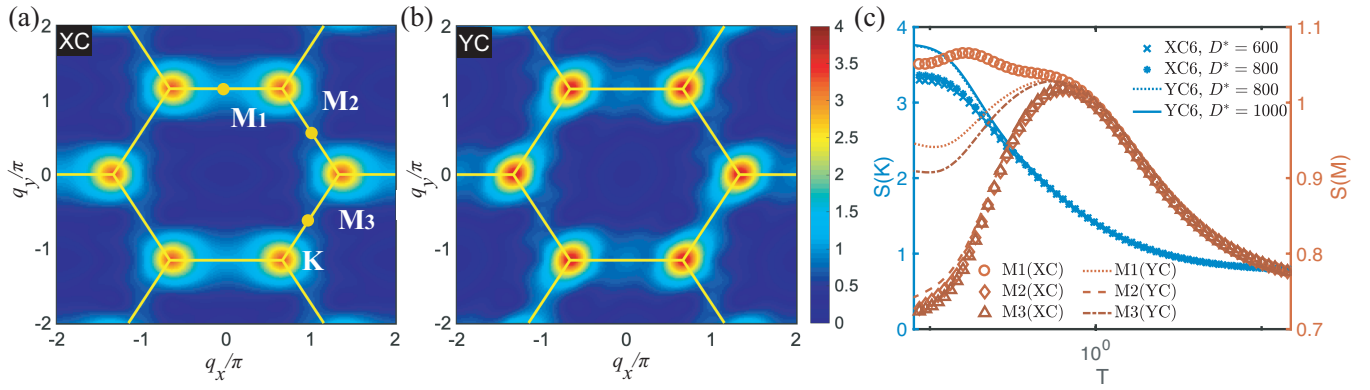


FIG. S7. (Color online) Comparison of structure factor between (a) $\text{XC6} \times 12$ and (b) $\text{YC6} \times 12$ geometries at $T = 0.103$. The direction along the cylinder corresponds to q_x and q_y , respectively. XC6 shows a higher intensity around M_1 which indicates a tendency to form stronger bonds around the circumference of the cylinder, i.e., stripe order. Consequently, XC6 has a lower $S(\mathbf{K})$ as compared to YC6, shown more explicitly in (c).

cases, there exist two M points (M_1 and M_3) which have strong intensity, while the remaining one, $S(M_2)$, is weak at low temperatures, although all three M points have anomalous enhancement at T around T_h , due to RLE activation. In XC6, there is one strong $S(M_1)$ as compared to weaker M_2 and M_3 points, indicating a strong tendency for stripe order [see also Fig. S4(d)], which is largely absent in YC6 case. Consequently, the strength of the K -point correlations in XC6 is impaired as well compared to the YC6 case [see Fig. S7(c)]. The situation here is thus opposite to the width $W = 4$ case, where YC4 shows a stripe phase, whereas XC4 does not.

Internal energy

In Fig. S8, we analyze the internal energy per site, $u(T) \equiv \frac{1}{N} \langle H \rangle_T$ with $c_V(T) \equiv \frac{\partial u}{\partial T} = -\beta \frac{\partial u}{\partial \ln \beta}$ [20], versus temperature and compare it to the ground state DMRG results on the same geometry. We show data for various geometries, including the $\text{YC6} \times 12$, $\text{OS6} \times 6$, and small $\text{YC4} \times 8$ lattices. It can be observed that the energy data are well converged with bond dimension $D^* = 1000$ (for YC6 and OS6) and $D^* = 400$ (YC4), which correspond to nearly $D \sim 4 \times D^*$ in terms of $U(1)$ states (see legend).

At low temperature, the $u(T)$ curves already closely approach the zero-temperature limits u_g [horizontal markers Fig. S8(a)] obtained by ground state density matrix renormalization group (DMRG) calculations. For a strong comparison, we replot the same XTRG data in Fig. S8(b), but now relative to the DMRG ground state energy u_g on a log-log plot. The data for

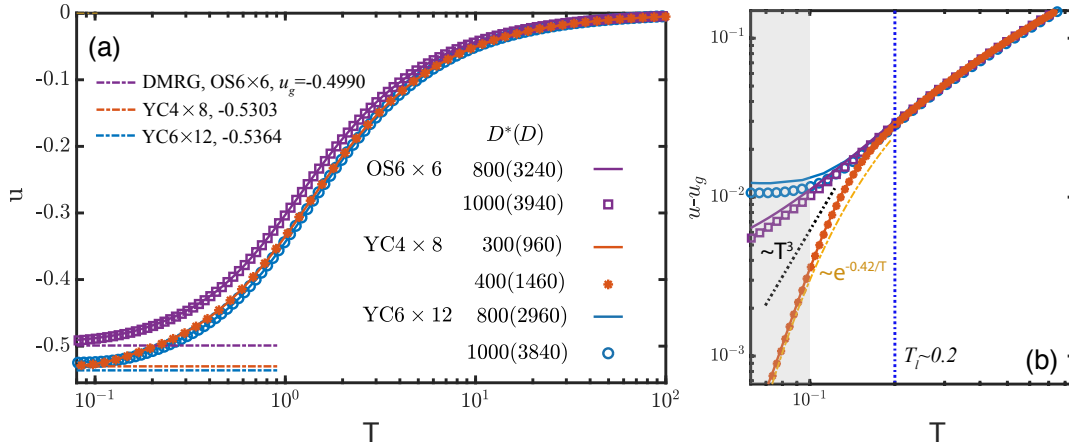


FIG. S8. (a) Internal energy, u vs. T , on YC6 \times 12, OS6 \times 6, and YC4 \times 8 lattices. The legend specifies the number of multipliers D^* followed by the corresponding number of $U(1)$ states. DMRG data u_g (horizontal markers) represent ground state results where we kept up to $D^* = 2000$ SU(2) multipliers. (b) Same data as in (a) but relative to u_g on a log-log plot, from which suggests algebraic convergence for OS6 and YC6. The latter (YC6, blue), however, is not yet fully converged below $T \lesssim 0.1$ (dashed regime) since it still changes with D^* . In contrast, YC4 already shows *exponential* convergence to the ground state energy for the lowest temperatures which may already be attributed to the finite size energy gap, as indicated by the exponential fitting. The OS6 data (purple) exhibits a quasi-algebraic behavior below T_l . The black dotted line is a guide to the eye and indicates the expected $\propto T^3$ at low T for large enough systems [e.g., cf. Fig. S13].

the intermediate to large temperature regime, $T > T_l$, scales similarly for all boundary conditions (with minor offsets due boundaries). As T decreases below T_l , the YC4 data converges exponentially, in agreement with the stripe-phase scenario revealed in Ref. [20]. In contrast, the OS6 and YC6 data collapse onto each other down to temperatures well below T_l (here the upturn in the YC6 system (blue data) is attributed to finite- D accuracy). Note that from the OS6 data in Fig. S8(b), one may estimate an approximate power-law behavior.

System size dependence of low-temperature scale T_l

In Fig. S9 we provide the scaling of the lower characteristic temperature T_l vs. length L for various YC6 lattices. As L increases, the lower peak/shoulder structure only slightly shifts towards lower temperatures, while it also becomes more pronounced, suggesting stronger 120° correlations in the system [in accordance with $S(K)$ data in Fig. 3(e) in the main text].

In the inset of Fig. S9 we plot the estimated position for T_l vs. $1/L$, and also indicate the position of shoulder-like structure in experimental curves [37]. Note that there exists some arbitrariness in determining T_l from peak/shoulder structure, as reflected in the error bars. Furthermore, in order to reduce the finite-length effect in YC6 data, we take the difference between YC6 \times 12 and YC6 \times 9 data (divided by the 6×3 extra sites) as a YC6 “bulk” results, whose lower peak is even more pronounced and the corresponding T_l well agrees with experiments, up to error bars.

Correlation length vs. temperatures

Assuming the Ornstein-Zernicke form of the static structure factor $S(q) = S(q_0)/[1 + \xi^2(q - q_0)^2]$, in the close vicinity of the ordering momentum q_0 , this defines the correlation length [5, 6] as

$$\xi^2 \cong \frac{1}{2S(q)} \left. \frac{\partial^2 S(q)}{\partial q^2} \right|_{q=q_0} = \frac{c_{q_0}^2}{2S(q_0)} \sum_j r_{0j}^2 e^{-iq_0 \cdot r_{0j}} \langle \mathbf{S}_0 \cdot \mathbf{S}_j \rangle, \quad (\text{S12})$$

where $r_{0j} \equiv r_j - r_0$ with r_j the lattice location of site j , with j running over the whole lattice, and again r_0 fixed in the center of the system. The constant $c_{q_0}^2 \equiv \langle \cos^2 \alpha_{0j} \rangle \in [0, 1]$ accounts for an angular average with α_{0j} the angle in between q_0 and r_{0j} . In the present context of the TLH, we chose $q_0 = K$ as the ordering momentum which leads to $c_0^2 = 1/2$.

From Fig. S10, one observes that the correlation length ξ remains very short, in that it is below one lattice spacing down to temperatures even below $T_h \sim 0.55$ also for the wider systems, in agreement with HTSE-2D in the thermodynamic limit. At lower temperatures, the correlation length gets enhanced with increasing width W and length L . Given the very short correlation

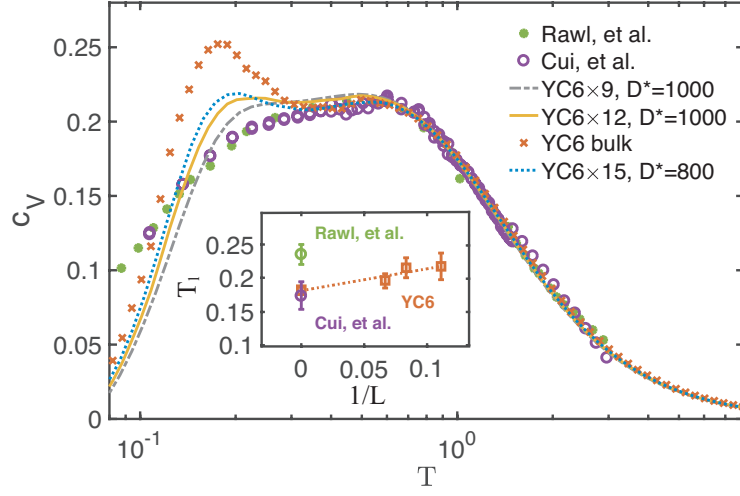


FIG. S9. Specific heat on YC6 for three different lengths, also compared to experimental data. The ‘YC6 bulk’ is obtained by subtracting YC6 \times 9 from YC6 \times 12 data, in order to reduce the effects from the open boundary. The inset shows the lower characteristic temperature T_l vs. $1/L$ with estimated error bars from the determination of T_l for the peak/shoulder structure. The data point at $1/L = 0$ is taken from ‘YC6 bulk’ curve which, indeed, approximately represents an extrapolation in $1/L \rightarrow 0$, as suggested by the dotted line. In particular, to determine T_l in experimental curves, we assume the shoulder is sitting on top of an approximately linear slope of the T_h peak: take T_l as the temperature where the curvature of $c_V(T)$ is maximally negative (i.e., the local minimum of the curvature around the shoulder). Note the sparse experimental data has been interpolated by 4th to 6th order polynomial fittings.

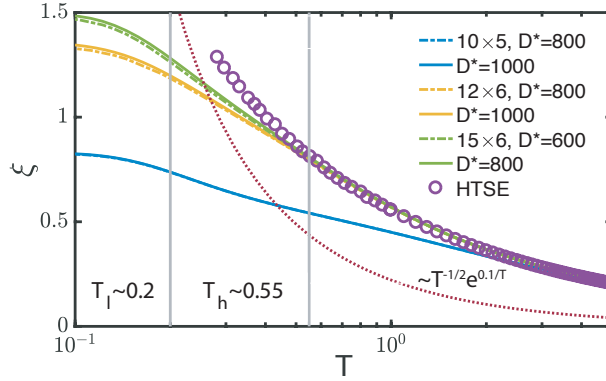


FIG. S10. Correlation length, ξ , on various YC cylinders, together with HTSE-2D data [5] for comparison. For reference, we also added the exponential increase $\xi \propto T^{-1/2} e^{T_l/2T}$ predicted by field-theoretical arguments (red dotted line) [9].

length of just a very few lattice spacings for $T_l < T < T_h$, incipient order can be ruled out in this intermediate regime. Instead, we associate this regime with activated RLEs (with minima at M), which suppresses the long-range order formation at K and thus leads to a short ξ . As temperature is lowered further, the correlation length ξ is expected to increase exponentially. As for our XTRG data, ξ keeps increasing down to $T \sim 0.1$, where it saturates due to the finite system size.

Entanglement spectra vs. temperatures

In Fig. S11, we analyze the ‘renormalization-group’ flow of the MPO entanglement spectra of the thermal state, $\rho(\beta)$ vs. the logarithm of the energy scale T , for a vertical cut across the middle of a YC6 \times 12 system, with focus on the two temperature scales T_l and T_h . This is significantly more detailed than the single number in terms of the MPO entanglement entropy S_E , e.g., as analyzed in Fig. 3(f) in the main paper. The entanglement spectra are also derived from the normalized ‘purified’ thermal state $|\rho(\beta)\rangle$ and its reduced density matrix $\mathcal{R}(\beta)_{I,I'} \equiv \sum_J |\rho_{I,J}\rangle \langle \rho_{I',J}|$ [20], where I, J represent degrees of freedom in left and right half of the system, respectively, and β is the inverse temperature. Then, the entanglement spectrum, \tilde{E}_S , at a given inverse temperature, β , is obtained by diagonalizing $\mathcal{H}_{ES} \equiv -\ln \mathcal{R}$. These are analyzed relative to their ‘ground-state energy’,

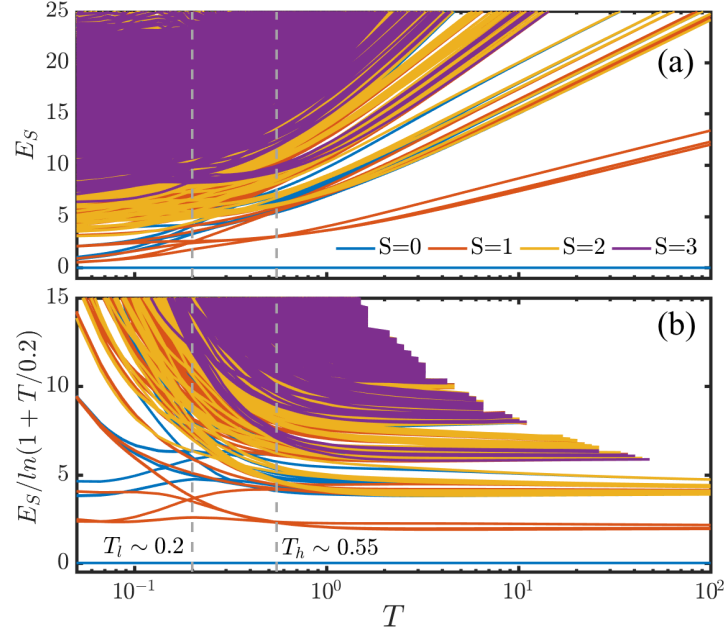


FIG. S11. (Color online) (a) Entanglement spectrum, E_S , across a vertical cut in the middle of a $YC6 \times 12$ system versus temperature T , where the color differentiates the $SU(2)$ spin symmetry sectors as indicated in the legend. Two temperature scales $T_l \sim 0.2$ and $T_h \sim 0.55$ are indicated with the grey dashed lines. (b) The same E_S data, yet scaled by $\ln(1 + T/a)$ with $a \sim T_l$. With this the high temperature spectra in (a) with $E_S \sim \ln T$ [20] become horizontal lines. At low $T < T_l$, empirically, the chosen scale factor $1/\ln(1 + \frac{T}{T_l}) \sim 1/T$ still represents a sensible scaling for the lowest levels, thus suggesting $E_S \sim T$ there.

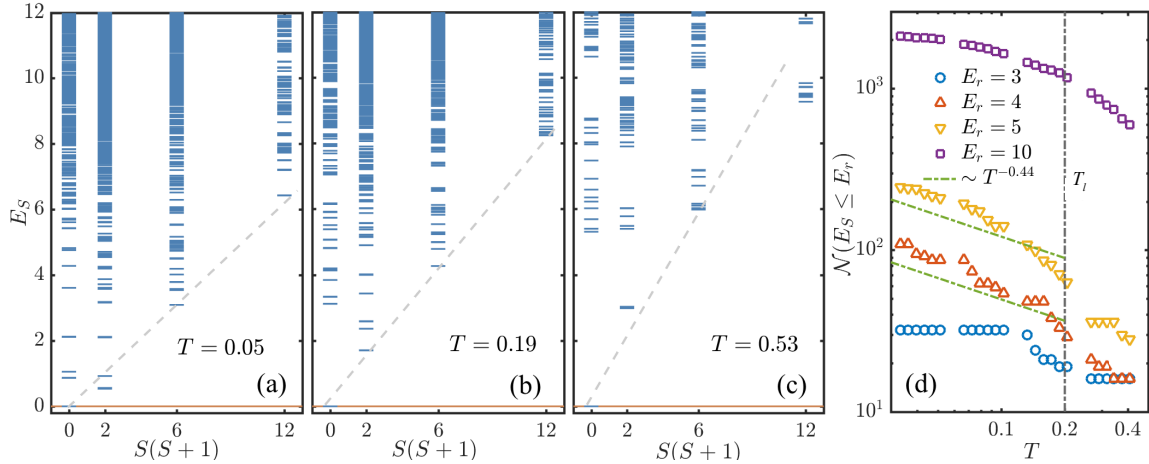


FIG. S12. (Color online) Entanglement spectrum (E_S) of entanglement Hamiltonian \mathcal{H}_{ES} with $SU(2)$ spin quantum number S at (a) $T = 0.05$, (b) $T = 0.19 \simeq T_l$, and (c) $T = 0.53 \simeq T_h$. The dashed lines are guide for eyes, indicating the increasing slopes of the ‘‘towers’’ with increasing temperatures. (d) Counting the number of states $\mathcal{N}(E_S \leq E_r)$ for $E_r = 3, 4, 5, 10$, at various temperatures. It is observed that \mathcal{N} increases as T decreases, and for a range of intermediate energies, say, $E_r = 4, 5$, \mathcal{N} scales approximately polynomially vs. T for $T < T_l$, with $\sim T^{-0.44}$ (see text) shown as guide to the eye.

i.e., $E_S \equiv \tilde{E}_S - E_0$.

In the entanglement spectra E_S in Fig. S11, the different symmetry sectors of the MPO virtual bond states are differentiated by color as indicated in the legend. We show eigenstates for each spin symmetry sector, up to a largest ‘energy’ $E_S \leq 25$, which corresponds to a weight in the density matrix as low as $\geq e^{-25} \sim 10^{-11}$. From Fig. S11, we can see that, while in the high temperature regime the levels in E_S are rather far apart (i.e. the MPO is close to a product state), they become much more dense with decreasing temperature. They show systematic qualitative changes, and in particular line-crossings in the ‘low-energy sector’ around T_l and T_h . For $T < T_l$, the entanglement spectra show a systematic (algebraic) approach towards the ‘ground

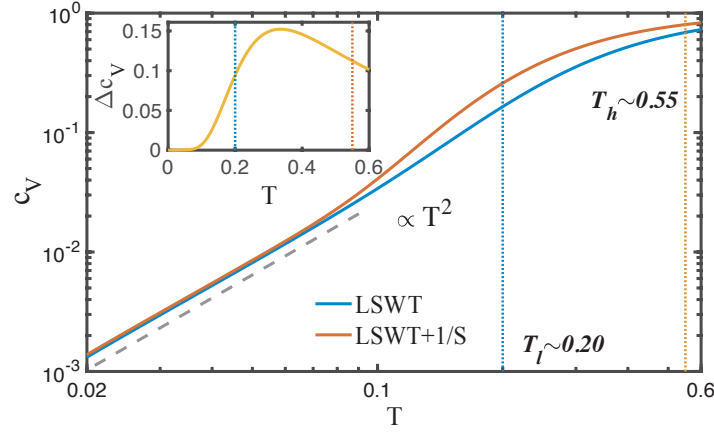


FIG. S13. (Color online) Low-temperature specific heat c_V from the spin wave analysis, with and without $1/S$ corrections [41], where the gray dashed line indicates the T^2 behaviors of c_V at low T due to the linear spin wave dispersion $E_k \propto k$ for small k . Inset shows the difference between the two approximations. The vertical markers indicate the two energy scales T_l and T_h as specified.

state’, with Fig. S11(b) roughly suggesting $E_S \sim T$ for the lowest levels once $T < T_l$. These distinct behaviors of E_S in different temperature regimes are consistent with the existence of two temperature scales.

In Fig. S12(a-b), we study the spectroscopy of the entanglement Hamiltonian \mathcal{H}_{ES} . The entanglement levels are plotted with respect to different symmetry labels from $S = 0$ up to $S = 4$, at $T = 0.19$ and 0.05 , respectively. As indicated by the gray dashed lines, the lowest level in each symmetry sector decreases, roughly algebraically as we cool down the system, while also the slope systematically decreases. As a consequence, the number of states with weights $E_S < E_r$, denoted by $\mathcal{N}(E_S \leq E_r)$, increases as T decreases. We plot $\mathcal{N}(E_S \leq E_r)$ in Fig. S12(d) with $E_r = 3, 4, 5, 10$. From this we observe that $\mathcal{N}(E_S \leq E_r)$ increases roughly polynomially when $T \leq T_l$, indicated by the green dashed lines. If furthermore, we assume rather heuristically that for intermediate E_r , say, $E_r = 4$ or 5 , each level in the range $E_S \leq E_r$ contributes crudely equally to the thermal entropy S_E of the entanglement Hamiltonian \mathcal{H}_{ES} system, this is consistent with an expected log-scaling of the entanglement entropy, $S_E \sim \ln \mathcal{N} \propto a_{\mathcal{N}} \ln \beta + b$. And, indeed, this hand-waving argument agrees with the scaling $S_E \propto a \ln \beta + b$ for $T \leq T_l$, as observed and discussed with Fig. 3(f) in the main text, even with roughly consistent slope $a_{\mathcal{N}} \approx a = 0.44$, also shown in Fig. S12(d) as guide to the eye.

Spin wave analysis

Linear spin wave theory (LSWT) can very well capture the 120° order in the ground state of TLH [29, 30, 46]. It is thus also believed that LSWT is able to describe thermodynamics at very low temperatures. Here we take the spin wave spectra with and without $1/S$ corrections [Eq. (12) from [41]], compute the specific heat according to the conventional Bose-Einstein distribution of magnon gas, and draw a comparison to our two-temperature-scale scenario.

In Fig. S13, we can see that the c_V curve with $1/S$ corrections also exhibit a “shoulder-like” structure at around T_l , below which it gradually changes into a T^2 scaling, coinciding there with pure LSWT results at low T .

The $1/S$ correction gives rise to the difference Δc_V which, as manifested in the inset of Fig. S13, strongly affects the intermediate temperature regime in between T_l and T_h . Δc_V starts to decrease rapidly below $T \sim T_l$, and the influences of RLEs as well as other renormalization effects in the spectrum due to $1/S$ corrections are largely absent below $T = 0.1$. This is consistent with our spin structure factor as discussed with Fig. 3(c-e), where S_M , representing the activation of RLEs, also becomes clearly weakened below T_l .

The LSWT analysis of c_V and its $1/S$ correction in Fig. S13 thus further confirms the existence of two temperature scales, and, in particular, the lower one T_l . Overall, Fig. S13 provides useful complementary thermal data to our finite-size XTRG results.

Chiral Correlations on YC4

This section complements the analysis of chiral correlations in Fig. 5 in the main paper, in that we focus on the case of YC4 which is special, in that T_l^* scales to zero as $L \rightarrow \infty$ (hence the asterisk with T_l). From Fig. S14 we observe that short-ranged

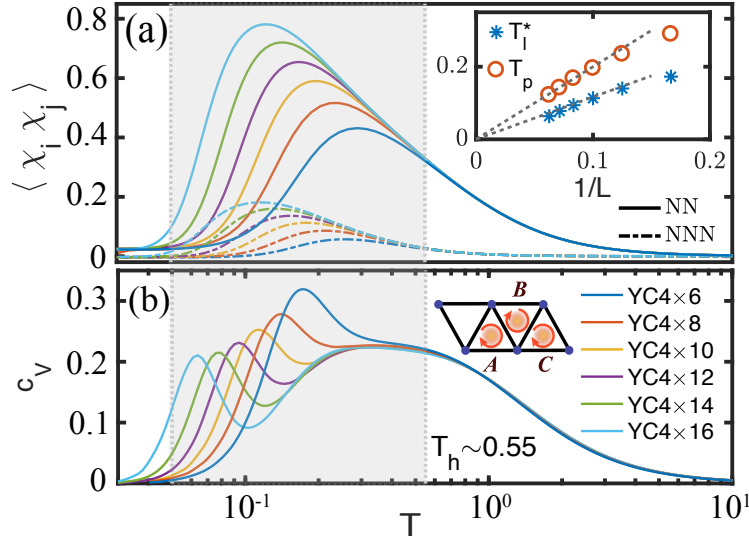


FIG. S14. (Color online) (a) Chiral correlations compared to (b) specific heat c_V in YC4 for various lengths L . In (a) we consider correlations between nearest- (NN) and next-nearest neighboring (NNN) triangles in the system center [i.e., using $i = A$ and $j = B, C$ as shown in the inset of (b) with the triangles taken in the system center [cf. Fig. 1]. The disappearance of the low-energy regime for $1/L \rightarrow 0$ is specific to YC4 [20]. The inset shows finite size scaling of the peak position, T_p , in the chiral correlations $\langle \chi_i \chi_j \rangle$, as well as of the temperature scale, T_l^* , derived from the lower-temperature peak in c_V from (b).

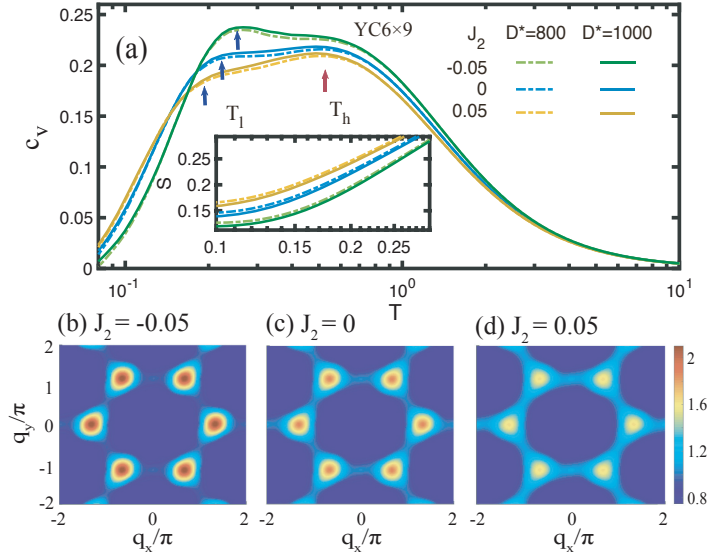


FIG. S15. (Color online) (a) Specific heat, as well as thermal entropy (inset), of J_1 - J_2 TLH, with $J_2 = -0.05, 0$, and 0.05 , on $YC6 \times 9$ geometry. (b,c,d) show the structure factors at $T \simeq 0.53$ near the high temperature scale T_h .

(NN and NNN) chiral correlations build up and become strong at intermediate temperatures, $T_l^* \lesssim T \lesssim T_h$. Clearly, the peak at T_p in the chiral correlations [Fig. S14(a)] correlates with the low-energy scale T_l^* derived from c_V [Fig. S14(b)]. Below T_l^* , chiral correlations become negligibly small, which is also directly confirmed by DMRG simulations (not shown). While YC4 also enters an anomalous liquid-like regime for $T < T_h$, it becomes a stripe phase below a low-energy scale T_l^* which diminishes to zero in the thermodynamic limit as demonstrated in the inset to Fig. S14(a) [20]. This is qualitatively different from $T_l \sim 0.20$ in wider cylinders and strips, where it becomes a stable temperature scale vs. various system sizes and boundary conditions as shown and discussed with Fig. 2(a). Importantly, Fig. S14 demonstrates that the peak T_p in the chiral correlations closely follows the low-energy scale T_l^* derived from the specific heat. In this sense we conclude that they can be ascribed to the same crossover scale that separates the low-energy (here stripe) order from the intermediate regime and, moreover, that finite chiral correlations constitute a characteristic property of the intermediate regime.

TUNE SPIN FRUSTRATION BY DEFORMING THE TRIANGULAR-LATTICE HEISENBERG MODEL

J_1 - J_2 Triangular lattice Heisenberg model

To shed further light on the two-temperature-scale scenario, we deform the TLH by including a small but finite next-nearest coupling J_2 ,

$$H = J_1 \sum_{\langle i,j \rangle} \vec{S}_i \cdot \vec{S}_j + J_2 \sum_{\langle\langle i,j \rangle\rangle} \vec{S}_i \cdot \vec{S}_j, \quad (\text{S13})$$

having $J_1 \equiv J = 1$. A small AF coupling $J_2 > 0$ adds frustration, and hence suppresses 120° ordering on a three-sublattice configuration [31–34], while $J_2 < 0$ reinforces the ferromagnetic correlations between two spins on the same 120° sublattice.

In Fig. S15 we compare the specific heat c_V of $\text{YC6} \times 9$, for $J_2 = 0$ with $J_2 = \pm 0.05$. From the temperature dependence in Fig. S15(a) we can see that as we change J_2 from -0.05 to 0.05 , the T_l peak systematically shifts to lower temperatures, while at the same time, it weakens. In contrast, the broad peak at T_h keeps its position while varying J_2 . The overall downward shift for temperatures $T \gtrsim 0.2$ and upward shift for very small temperatures suggests that with increasing J_2 , more entropy is transferred to lower temperatures. Indeed, as shown in the inset of Fig. S15(a), compared to $J_2 = 0$ case, thermal entropy S at $T = 0.1$ is increased (decreased) by $\sim 15\%$, when $J_2 = 0.05$ (-0.05) is introduced.

The sensitivity of the structure factor on J_2 is analyzed in Figs. S15(b-d). As expected, increasing J_2 significantly reduces the weight $S(K)$, but enhances the weight $S(M)$. This is consistent with dynamical calculations of the J_1 - J_2 TLH [68], as well as that includes spin XXZ anisotropy [67], which show that RLEs are renormalized downward by increasing $J_2 > 0$, giving rise to an extended dispersive continuum above the “roton” minimum.

Frustrated square-lattice antiferromagnet

Besides adding J_2 in to TLH, we can also deform the Hamiltonian towards the square lattice Heisenberg (SLH) model via a tuning parameter J_t where $J_t = 1$ corresponds to the TLH, and $J_t = 0$ to the SLH. The corresponding Hamiltonian of the frustrated SLH is given by,

$$H = J \sum_{\langle i,j \rangle} \vec{S}_i \cdot \vec{S}_j + J_t \sum_{\langle\langle i,j \rangle\rangle} \vec{S}_i \cdot \vec{S}_j, \quad (\text{S14})$$

where $\langle \cdot, \cdot \rangle$ denotes nearest-neighbor, and $\langle\langle \cdot, \cdot \rangle\rangle$ next-nearest neighboring pairs of sites along one of the diagonals only [e.g., as depicted in the inset to Fig. S16(c)]. Their respective coupling strengths are given by J and J_t , where again $J = 1$ sets the unit of energy, unless specified otherwise. The system features square lattice Néel order at $T = 0$ for $J_t = 0$, leading to low- T RC behavior [35]. Finite $J_t > 0$ introduces frustration in the system, which leads to an abrupt onset of an incommensurate spiral wave at some critical $J_t^c \sim 0.79$ [28]. For the isotropic TLH at $J_t = 1$ this turns commensurate and yields the familiar 120° order. Our results for the SLH on a 6×12 cylinder (i.e. $L = 2W = 12$) are summarized in Fig. S16, where we vary J_t from 0 to 1 (see legend), with $D^* = 500$ multiplets kept.

The specific heat c_V is shown in Fig. S16(a). The tracked lowest temperature scale, i.e., global peak position for $J_t \leq 0.8$ and the position of the lower shoulder for $J_t > 0.8$, is plotted as ‘ T_l ’ in the inset. This scale starts from about $T_l = T_h \sim 0.6$ for $J_t = 0$ (i.e., the pure SLH case). While T_l decreases gradually with increasing J_t , at the same time a shoulder emerges at the original peak position T_h which only marginally moves to smaller values. At around $J_t \simeq 0.8$, the single peak in the specific heat for small J_t is about to fully split into two peaks. There T_l has already nearly also reached its final value of 0.2 for $J_t = 1$, i.e., the isotropic TLH. Interestingly, the critical value for which ground state calculations observe the onset of incommensurate correlations, $J_t^c \sim 0.79$ [28], roughly coincides with the J_t for which a well separated two-peak structure has developed at finite T (for the finite size systems here even with a minimum in between), where T_l is already also close to its final value of 0.2 for the TLH.

To understand the physical meaning of the temperature scales and their behaviors under various J_t , we look at the static structure factors, $S(C)$ and $S(M)$, in Fig. S16(b). The points C and M in reciprocal space are pointed out in the inset. We observe that, for $J_t \lesssim J_t^c$, the AF magnetic order [at $C = (\pi, \pi)$, i.e., Néel order] melts most rapidly at the characteristic temperature T_l . The magnetization per site may also be estimated in the present case by $m \approx \sqrt{S(C)/N}$ (note the slightly different normalization due to angular average as compared to the TLH). For $J_t = 0$, this yields $m \sim 0.39$ which overestimates the thermodynamic limit $m \sim 0.31$ [4] due to finite-size effects.

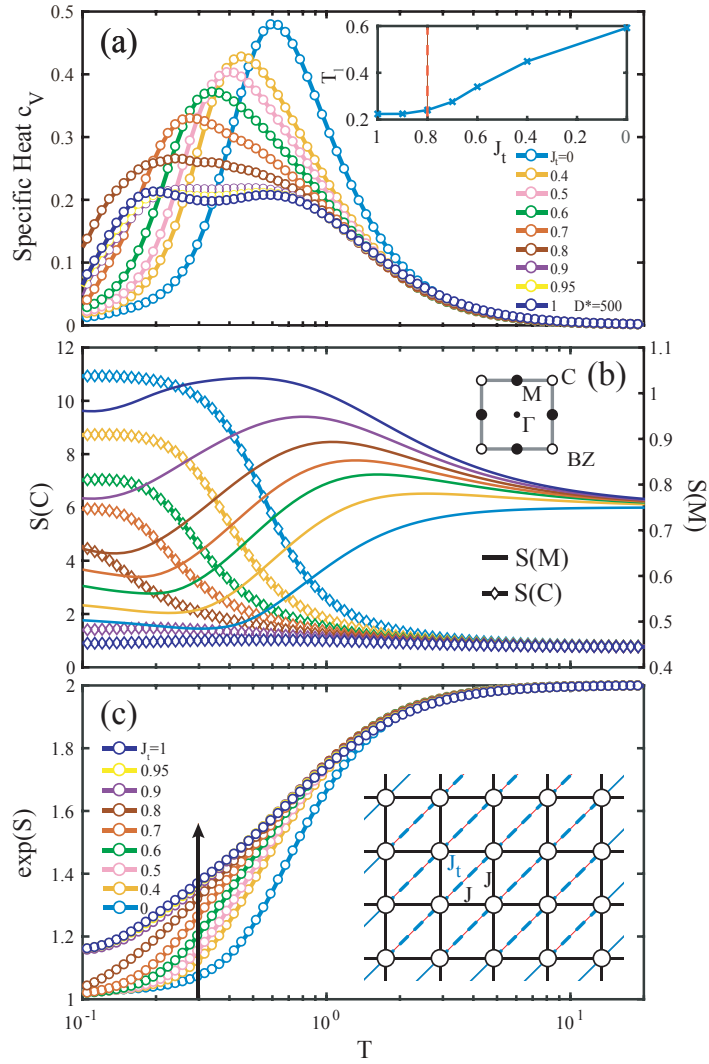


FIG. S16. (Color online (a) Specific heat data for the frustrated SLH on a 6×12 cylinder with J_t varied from 0 to 1, keeping up to $D^* = 500$ multiplets [1790-2010 U(1) states]. The inset traces the low-temperature peak (or shoulder) in the c_V curves. (b) Static structure factor $S(q)$ at $C = (\pi, \pi)$ (lines with markers) and $M = (0, \pi)$ (solid lines). The constant offset towards large T is a trivial finite size effect: it is the same for $S(M)$ and $S(C)$ (note the significantly different vertical scales for $S(C)$ [left axis] and $S(M)$ [right axis]) and comes from the $r_j = r_0$ contribution in the definition of the structure factor, which gives a constant $\langle S^2 \rangle_T = \frac{3}{4}$. (c) Thermal entropy S decreases from $\ln 2$ as T is lowered. The thermal entropy moves to larger values as the frustration is turned on via J_t .

The stable large energy scale at T_h relates to different physics, here argued to be RLEs. This argument can be solidified by analyzing the structure factor at the point $M = (0, \pi)$ which, indeed, shows anomalous enhancement at intermediate temperatures for finite J_t . Note that the position of the maximum in $S(M)$ changes from ~ 1.5 for $J_t = 0.6$ to the value of $T_h \sim 0.55$ itself for $J_t = 1$.

In Fig. S16(c), finally, we still present data for the thermal entropy S for various J_t values. From this we can see an anomalous enhancement of the entropy as $J_t \gtrsim J_t^c \sim 0.8$. It is remarkable to find the zero temperature commensurate-incommensurate transition also reflected here as a (residual) entropy enhancement in our thermal calculations at our lowest temperatures.

In summary, the specific heat as well as the static structure factor data in Fig. S16 provide further strong support for the emergence of a two-temperature-scale scenario at sufficiently large frustration J_t , including the $J_t = 1$ TLH.